

Biomass burning combustion efficiency

Understanding spatial resolution and
environmental drivers in biomass burning
combustion efficiency using TROPOMI satellite data

AESM7000: Master Thesis

Ayush Kumar Jha



Netherlands Institute for Space Research



Biomass burning combustion efficiency

Understanding spatial resolution and
environmental drivers in biomass burning
combustion efficiency using TROPOMI satellite
data

by

Ayush Kumar Jha

Student Number: 5711673

to obtain the degree of Master of Science
at the Delft University of Technology.

Thesis Committee: Steven van der Linden (TU Delft, chair & supervisor)
Pepijn Veeffkind (TU Delft)
Joris Timmermans (TU Delft)
Ivar van der Velde (supervisor, SRON)
Helene Peiro (supervisor, SRON)
Project Duration: January, 2024 - July, 2024
Faculty: Civil Engineering and Geosciences, TU Delft

Abstract

In recent years, record-breaking wildfires have occurred globally, with projections indicating a dramatic increase in their frequency and intensity in the future. These wildfires present serious risks to the environment by releasing harmful pollutants and various greenhouse gases, which significantly contribute to air pollution and climate change. To accurately predict emissions of such gases, a comprehensive understanding of combustion efficiency is essential. Due to TROPOMI's capability to measure trace gases such as NO₂ and CO with high spatial resolution and global coverage, it has been used in various studies to analyse combustion efficiency. The study used NO₂ and CO column concentrations measured by TROPOMI to estimate Mole Density Ratio (MDR), which is a proxy of combustion efficiency, over two devastating wildfires that occurred in California in 2020. By using TROPOMI data, aggregated to various resolutions using the super-observation approach, the study assessed the spatial and temporal limits of TROPOMI-derived MDR. It evaluated changes in MDR values across various vegetation types by integrating higher resolution land classification data from MODIS. Additionally, it explored the relationship between MDR and environmental indicators such as drought conditions and soil moisture. Super-observations resulted in significantly different MDR values with those estimated at TROPOMI resolution. The findings indicated that there was loss of information regarding MDR when super-observations were used. Furthermore, there was no clear link found on the impact of environmental factors such as soil moisture and drought conditions on MDR. Finally, a detailed land use characterisation provided deeper insights into the effect of burning various types of vegetation on the MDR. However, to be able to fully interpret the effect of super-observations and environmental factors on MDR, a more extensive analysis is suggested.

Contents

Abstract	i
1 Introduction	1
2 Methodology and Data	6
2.1 Methods	6
2.1.1 Calculation of background values of NO ₂ and CO	6
2.1.2 Calculation of Mole Density Ratio (MDR)	8
2.2 Datasets	8
2.2.1 TROPOMI Retrievals	8
2.2.1.1 Nitrogen dioxide (NO ₂)	8
2.2.1.2 Carbon monoxide (CO)	9
2.2.1.3 Super-observations	9
2.2.2 Environmental Indicators	10
2.2.2.1 Standard Precipitation-Evapotranspiration Index (SPEI)	10
2.2.2.2 Soil Moisture (SM)	10
2.2.3 Land Cover Data	11
2.2.3.1 Global Fire Emission Database (GFED)	11
2.2.3.2 Moderate Resolution Imaging Spectroradiometer (MODIS)	11
2.2.4 Moderate Resolution Imaging Spectroradiometer (MODIS) active fire product	12
2.2.5 ERA5 Wind	13
3 Results	14
3.1 Mole Density Ratio	14
3.2 Mole Density Ratio (MDR) and Environmental Indicators	20
3.2.1 MDR link with Standard Precipitation-Evapotranspiration Index (SPEI)	20
3.2.2 MDR link with Soil Moisture (SM)	21
3.3 Mole Density Ratio (MDR) and Land Cover	23
3.3.1 MDR link with GFED Land Cover	23
3.3.2 MDR link with MODIS Land Cover	25
3.3.3 Daily MDR link with MODIS Land Cover	27
4 Discussion and Outlook	28
References	30
A Appendix	33
A.1 Data Summary	33
A.2 Monte Carlo Simulation	36
A.3 Wind Rose Diagrams	36

1

Introduction

Several record-breaking wildfires have been reported across the globe in recent years, some of which have reached unprecedented scales and durations. Examples include wildfires in Canada, Greece and Australia in 2023 [1], and the United States in 2020 [2]. According to a report by the United Nations Environment Programme, climate change and variations in land use are expected to lead to more frequent and intense wildfires globally. The report forecasts a potential increase in extreme fires of up to 14% by 2030, 30% by the end of 2050, and 50% by the end of the century [3]. Furthermore fires triggered by heat are anticipated to increase substantially [4] due to shifting climatic conditions characterised by rising heatwaves and drought occurrences [5] which is evident by the recent increase in large wildfires associated with dry conditions, particularly in the Western USA [6].

Wildfires pose significant risks to human health due to the substantial rise in concentrations of harmful pollutants released in wildfire smoke [7]. The smoke produced by fires contains aerosols such as volatile organic compounds, particulate matter (PM) and various trace gases such as carbon monoxide (CO), nitrogen oxides (NO_x). In addition, greenhouse gases such as carbon dioxide (CO₂) and methane (CH₄) are also emitted that induce climate change and deteriorate quality of air [8], [9]. There have been various studies on the negative economic and social effects caused by products emitted during wildfires. Such wildfires result in growing economic and public health challenges [10]. The total healthcare expenses, in the United States, associated with mortality and morbidity resulting from exposure to wildfire-related PM_{2.5} are estimated to be between \$11 billion and \$20 billion (2010\$) per year [11].

Although wildfires cause significant rise in concentrations of pollutants, there is still considerable uncertainty in the exact values [12]. Emission factors (EFs) relate the mass of pollutants emitted per unit of burnt dry biomass. These are essential inputs for emission models used to develop emission inventories (EI), which help in comprehending the impact of wildland fires on the atmosphere and climate. These EFs can vary widely depending on fuel composition, fire type and combustion conditions [13]. Part of the uncertainties in emission estimates is due to the fact that they are not only broadly defined, but also that they are assumed to be constant in space and time.

The relationship between emission factors and combustion efficiency, which is the fraction of burnt fuel carbon converted to CO₂, shows considerable variability [14]. The study by [15] mentions that ground based measurements of emission factors are limited by the spatial and temporal representativeness. Satellite based data have the advantage of filling the gap. Shankar et al. [7] states that it is crucial to develop region specific approaches for creating wildfire emissions inventories (EIs) that consider variations in climate and societal factors. This is essential for improving the ability to predict changes in wildfire emissions and their impacts on air quality as well as for effectively managing wildfires and mitigating associated health risks over the long term. The scope and duration of such studies before the satellite era were significantly restricted. However, significant progress has been made in detecting atmospheric pollution using satellite technology since then [16]. New satellite missions and integration of diverse data sources could enhance the parameterisation of fuel consumption in models. For instance, combining data from the extended period of Moderate Resolution Imaging Spectroradiometer (MODIS) observations, which has a detailed land classification system, with more recent instruments has the potential to decrease certain uncertainties [17].

The Tropospheric Monitoring Instrument (TROPOMI), on board the satellite Sentinel 5-P, is one of the recent satellite missions to enhance our understanding of the intensity, development and spatiotemporal fluctuations in the origins of trace gases and aerosols influencing both air quality and climate [18]. Various studies have demonstrated the capability of TROPOMI to analyse trace gases such as nitrogen dioxide (NO_2) and carbon monoxide (CO) emitted from wildfires. Van der Velde et al. [15] focused on comparing the atmospheric enhancements of NO_2 and CO measured by TROPOMI over different fire-prone ecosystems around the world. They aimed to understand combustion characteristics and improve global emission inventories for the fire modelling community to accurately predict fire emissions by quantitatively assessing the influence of biomass burning on atmospheric chemistry and climate. They used the ratio between the column enhancements of NO_2 and CO, termed as Mole Density Ratio (MDR), as a proxy for measuring the combustion efficiency (CE) of a fire. The analysis revealed distinct spatial and temporal patterns in the NO_2/CO ratio, indicating regional differences in combustion efficiency across the globe. The study discovered that variations in the emission factors of nitrogen oxides (NO_x) and CO are influenced by differences in biomass burning behavior, which are caused by the burning phase of the fire such as flaming versus smouldering combustion. Flaming combustion is characterised by high temperature oxidation of gas, occurring over the surface of the forest floor and is widely seen in grassland type of vegetation [15], [19]. On the other hand, smouldering combustion is low temperature oxidation of solid occurring both above and below forest floor [20]. It is a feature of forest type of vegetation (see Figure 1.1). Van der Velde et al. [15] concluded that the fraction of smouldering combustion is much larger for boreal forest fires and peatland fires. These types of fires cause a much larger increase in CO relative to NO_2 . Overall, the study suggested that TROPOMI measurements can provide new insights into biomass burning characteristics and combustion efficiency for different vegetation types.

While [15] studied combustion efficiency (CE) across various vegetation types globally using the Global Fire Emission Database (GFED), [21] analysed CE at a regional scale. They focused on different vegetation types in two counties in California affected by wildfires between August and October 2020, also using GFED data. They used TROPOMI retrievals of carbon monoxide (CO) and nitrogen dioxide (NO_2) column average densities to calculate combustion efficiency, using the same method used as [15], which was then used to indicate fire characteristics based on Global Fire Emissions Database (GFED) land use type. When comparing CE to change in vegetation type, they found that change in CE was linked to change in vegetation. They also highlighted the need for improved land cover maps to better attribute combustion efficiency to specific fuel source categories.

The study by [22] used TROPOMI retrievals of NO_2 and CO to analyse trace gas ratio of NO_2/CO , to understand the evolution of combustion conditions during wildfires. It focused on fifteen large wildfires in California, Oregon, and Washington during the 2020 and 2021 wildfire seasons. It observed a consistent decrease in trace gas ratio enhancements ($\Delta\text{NO}_2/\Delta\text{CO}$) as the wildfires progressed from more flaming to more smouldering combustion. This decrease was consistent across different fuel types. Furthermore, the study explored the influence of chemical transformations in the atmosphere on trace gas ratios, noting that the ratios varied as the bounding box size (domain used for calculating trace gas ratios) expanded. When comparing observed trace gas ratios at $1^\circ \times 1^\circ$ with those at $0.16^\circ \times 0.16^\circ$, the $\Delta\text{NO}_2/\Delta\text{CO}$ ratio was underestimated by 25 %, indicating the importance of accounting for combustion conditions in emission assessments. These findings show the potential of TROPOMI observations to enhance models and parameterisations for estimating emissions based on changing combustion dynamics.

TROPOMI, is thus promising but often satellites have a finer spatial resolution than the resolutions used by models leading to representativeness errors in the model. Super-observations refer to a technique used in remote sensing and satellite data analysis where data from multiple finer resolution grid cells are combined with weighted factors to produce a single data point at a coarser resolution grid cell. Miyazaki et al. [25] used this approach where Ozone Monitoring Instrument (OMI) and SCanning Imaging Absorption spectroMeter for Atmospheric CHartographY (SCIAMACHY) NO_2 data products available at finer resolution ($13 \times 24 \text{ km}^2$, $60 \times 30 \text{ km}^2$) were gridded to a resolution of $2.5^\circ \times 2.5^\circ$ which is almost equivalent to the resolution used by the global chemical transport model (CTM), Chemical Atmospheric GCM for Study of Atmospheric Environment and Radiative Forcing (CHASER). The study concluded that creating super-observations at a spatial resolution that matches the model grid can improve data assimilation by providing more representative data, potentially leading to a reduction in systematic errors within the model. In situations where standard observations were used, the data



(a) Flaming type of combustion [23]



(b) Smoldering type of combustion [24]

Figure 1.1: Different types of wildfire combustion

often showed significant representativeness errors and noise, particularly in polluted regions, which can constrain the effective and stable reduction of systematic errors in the model. Utilising the super-observation technique typically yielded data that were more representative and with less random error, hence the use of super-observations. Additionally, this approach reduces the computational costs of data assimilation by processing reduced data points [25]. However, there are certain limitations to this approach. It may not accurately capture small-scale and rapid changes in concentration variations. It also showed that biases in the satellite retrieval process and the settings of the model employed for data assimilation largely impact the estimated emissions' magnitude. In order to understand the effect of such super-observations on estimation of MDR, in this study, TROPOMI retrievals are regridded at different resolutions between $0.5^\circ \times 0.5^\circ$ and $0.25^\circ \times 0.25^\circ$.

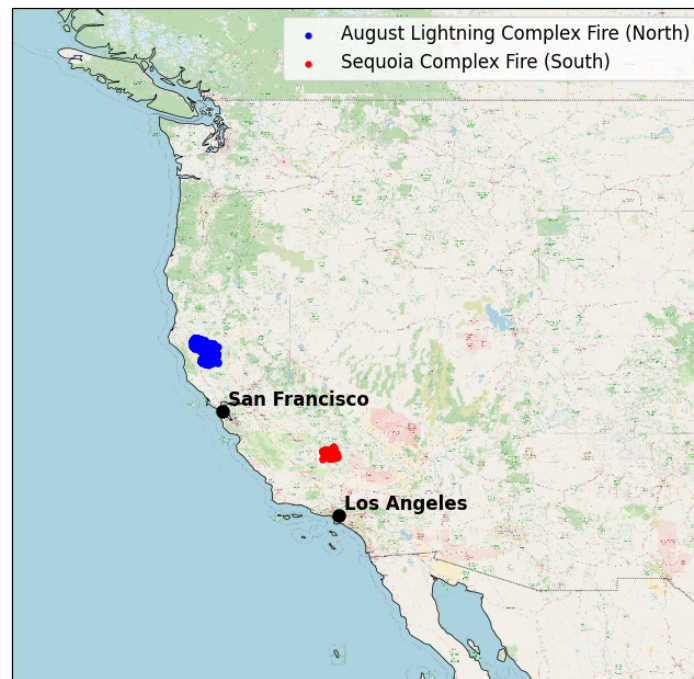


Figure 1.2: The figure indicates the location of the August Lightning Complex Fire and the Sequoia Complex Fire in the region of California, USA (2020). The blue and red markers denotes fire hotspots (obtained using MODIS active fire product) in the August Lightning Complex fire and Sequoia Complex fire respectively.

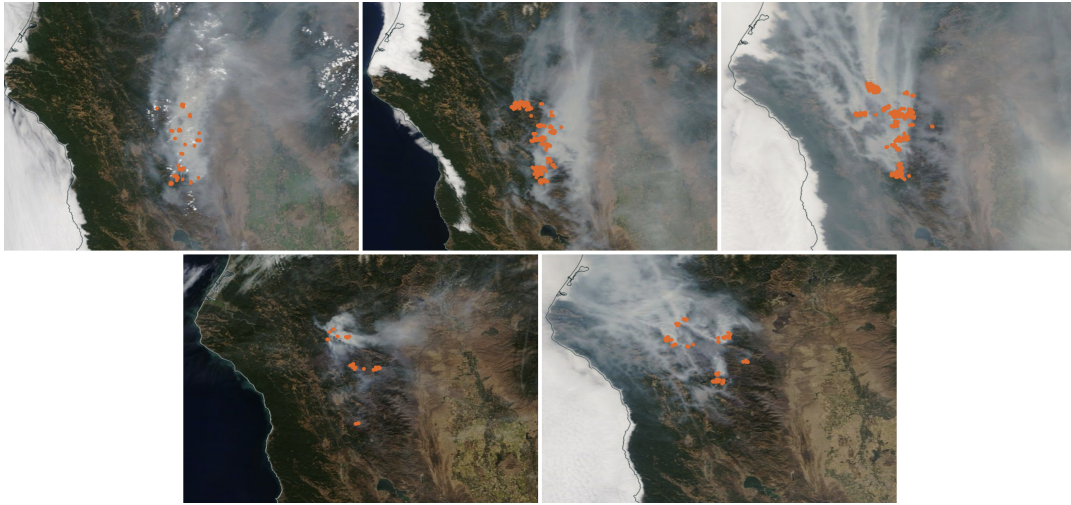


Figure 1.3: Progression of August Lightning Complex Fire, 2020 : This composite image shows the progression of wildfire activity in the August Lightning Complex Fire (considered northern region in this study). Each satellite image is marked with orange dots indicating fire hotspots. The top row represents the dates August 26th, September 4th, and September 13th, respectively. The bottom row shows the dates September 25th and October 6th. The increasing density and spread of hotspots highlight the escalation of the wildfire situation over time. The images have been taken from <https://worldview.earthdata.nasa.gov>



Figure 1.4: Progression of Sequoia Complex Fire, 2020 : This composite image shows the progression of wildfire activity in the Sequoia Complex Fire (considered southern region in this study). Each satellite image is marked with orange dots indicating fire hotspots. The top row represents the dates August 26th, September 4th, and September 13th, respectively. The bottom row shows the dates September 25th and October 6th. The increasing density and spread of hotspots highlight the escalation of the wildfire situation over time. The images have been taken from <https://worldview.earthdata.nasa.gov>

This research builds upon the work done by [15],[21] and focuses on the 2020 California wildfire season that witnessed the largest fires in the state's recorded history. Due to their relative positions, August Lightning Complex Fire is considered the northern region while Sequoia Complex Fire is considered the southern region in this study (see Figure 1.2 - Figure 1.4). The region of study is the same as that in [21]. While the study by [15],[21] used TROPOMI retrievals along with coarser GFED which has limited land use type for analysing MDR, this study aims to investigate how MDR is affected when TROPOMI data is gridded at different resolutions using the super-observations approach, along with the use of a higher resolution MODIS land use type. Starting from TROPOMI's native pixel resolution of $7 \times 7 \text{ km}^2$ for CO and $3.5 \times 7 \text{ km}^2$ for NO₂ column density at nadir to a gridded representation up to $0.5^\circ \times 0.5^\circ$, that is typically used in climate/meteorological models, the spatial and temporal limits of the TROPOMI derived MDR are investigated, determining the extent to which fire characteristics (CE) remain discernible from space. Furthermore, a higher resolution land classification data (MODIS) with several land use types is used to obtain a more detailed understanding of changes in MDR values across several types of vegetation. Specifically, this study aims to answer two research questions:

- What is the impact of spatial resolution of observed NO₂ and CO data on the ability to detect meaningful signals (significant changes) related to combustion efficiency (CE) by estimating Mole Density Ratio (MDR), as a proxy of CE?
- To what extent do land use characterisation and environmental factors such as droughts and soil moisture content impact biomass burning CE?

This thesis is structured as follows: a description of the used data and applied methodology is provided in Chapter 2. Chapter 3 subsequently presents the main results whereas the conclusions and outlook are included in Chapter 4.

2

Methodology and Data

2.1. Methods

2.1.1. Calculation of background values of NO₂ and CO

Firstly, wind components at each location of the fire hotspots are determined. The resultant of the wind components and its direction is calculated, followed by locating the background sampling region upwind of the fire hotspots.

Regarding the location of the background in the upwind direction, a distance is preferred such that it is close enough to catch characteristic of each fire region but far enough that the background is not influenced by the plume of nearby fire. Proximity of urban areas from the fires is also considered while choosing these distances to avoid contamination from anthropogenic sources of emissions. The fires in the northern region are spread apart and covered a larger area. In order to ensure that the background is not influenced by other fires of the same region, 90 km is considered far enough to remove the background. For the southern region, fires were closer to each other and covered a smaller area compared to the northern region, therefore, 30 km is considered close enough to be in the proximity of the region of interest, but far enough to not be influenced by other fires nearby. Such conditions were determined and used by [21], therefore, the same conditions are used in this study.

The coordinates of a location 90 km north and 30 km south, upwind of the fire hotspots, are calculated to determine the sampling location for background values as shown in Figure 2.1. This is done using Vincenty's formulae which are a pair of iterative techniques used in geodesy for computing the distance between two points on an ellipsoidal model of the Earth's surface. Furthermore, given the latitude and longitude of a point on the ellipsoid and geodesic distance, Vincenty's formulae can also be used to find the finishing point. This method was developed by Thaddeus Vincenty [26]. It is specifically designed for calculations based on the oblate spheroid shape of the Earth. Thomas et al. [27] recommends the use of Vincenty's formulae for geodetic calculations as it offers greater accuracy compared to distance calculation methods that assume a spherical earth, such as the great-circle distance approach.

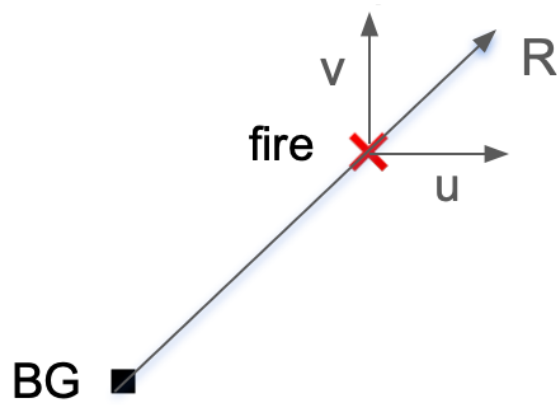


Figure 2.1: Determination of background sampling location : The red cross represents the location of a fire. The wind components at the location of the fire are indicated by u and v while R is the resultant wind vector. The background location is determined by a distance (90 km for the northern region and 30 km for the southern region) along the upwind direction, represented here by the black marker and denoted as BG.

2.1.2. Calculation of Mole Density Ratio (MDR)

The Mole Density Ratio (MDR) is the concentration equivalent of the emission factor ratio (EFR) which is a relative measure indicating the number of millimoles of NO_x released into the atmosphere per mole of CO. It provides a remotely sensed proxy for biomass combustion efficiency [15]. It is the ratio of the enhancements of column measurements of nitrogen dioxide (ΔXNO_2) and carbon monoxide (ΔXCO) and can be used to identify fire characteristics (see Equation 2.1). To prevent contamination from non combustion sources of emissions it is required to derive the regional enhancements in NO_2 and CO relative to the background for which a local sampling method is used. Van Der Velde et al. [15] used this method for regions where local fires and areas of higher concentration of trace gases were identified for which background column density upwind of the fires could be determined based on the wind direction. Once the location of the fires and the background is known, column densities of nitrogen dioxide ($X\text{NO}_{2_{fire}}$ and $X\text{NO}_{2_{BG}}$) and carbon monoxide ($X\text{CO}_{fire}$ and $X\text{CO}_{BG}$) are sampled at these locations. The difference of these values are the enhancements ΔXNO_2 and ΔXCO . Subsequently, a mean MDR is derived using Equation 2.1. The same method was also used by [21].

In this study, for each fire period considered, ΔXNO_2 and ΔXCO over fire hotspots are randomly sampled using a Monte Carlo simulation. This method provides a robust statistical estimate of the MDR values by repeatedly sampling and calculating mean ratios. This approach is further described in section A.2.

$$MDR = \frac{\Delta\text{XNO}_2}{\Delta\text{XCO}} = \frac{X\text{NO}_{2_{fire}} - X\text{NO}_{2_{BG}}}{X\text{CO}_{fire} - X\text{CO}_{BG}} \quad (2.1)$$

2.2. Datasets

2.2.1. TROPOMI Retrievals

The Tropospheric Monitoring Instrument (TROPOMI) is a spectrometer aboard the Sentinel 5 Precursor (S-5 P) satellite [18]. The S-5 P mission involves a single-payload satellite orbiting low earth that offers daily global data on concentrations of trace gases and aerosols essential for air quality, climate influence and ozone preservation. The satellite's payload is TROPOMI, developed collaboratively by the Netherlands and the European Space Agency (ESA). TROPOMI is equipped with bands spanning ultraviolet (UV), visible (VIS), near-infrared (NIR), and shortwave infrared (SWIR) wavelengths. It has a spectral resolution that varies from 1 nm in the shortest UV band, 0.5 nm in the intermediate bands and to 0.25 nm in the SWIR band. This wavelength selection enables the observation of crucial atmospheric constituents, including ozone (O_3), nitrogen dioxide (NO_2), carbon monoxide (CO), sulfur dioxide (SO_2), methane (CH_4), formaldehyde (CH_2O), aerosols and clouds. One notable feature of TROPOMI is its capability to provide simultaneous column densities for various trace gases, such as NO_2 and CO.

Nitrogen dioxide (NO_2)

Nitrogen dioxide (NO_2) has a short lifespan in the troposphere, ranging from hours to days, and its emission sources are unevenly distributed. As a result, the spatial and temporal patterns of NO_2 have significant variability. Therefore, enhanced spatial resolution, achieved by TROPOMI, is crucial for NO_2 monitoring as it enables the differentiation of concentration variations and facilitates more accurate quantification of emission sources [28].

The visible band between 405 nm and 465 nm can be used for observations of NO_2 and is observed globally on a daily basis, with a spatial resolution of $3.5 \times 5.5 \text{ km}^2$ in nadir ($3.5 \times 7 \text{ km}^2$ before the 6th of August 2019). The NO_2 retrieval method utilises the Differential Optical Absorption Spectroscopy (DOAS) technique [29] and is a modified version of the algorithm employed in DOMINO [30]. During the retrieval process, NO_2 slant columns are determined from the measured spectra using the DOAS method. Subsequently, the tropospheric component of these slant columns density is distinguished from the stratospheric component. Finally, the tropospheric slant columns are converted into vertical columns of NO_2 using the tropospheric air mass factor (AMF) from the chemistry transport model TM5-MP. Bias estimates for tropospheric NO_2 meet the mission requirement of less than 50 %, while those for stratospheric NO_2 meet the requirement of less than 10 % (see Table 2.1). As a user guideline for the data quality, a quality assurance value is given with the data. It is recommended to only use those pixels with a quality assurance value of above 0.75 (0.5 in case cloud covered scenes are of

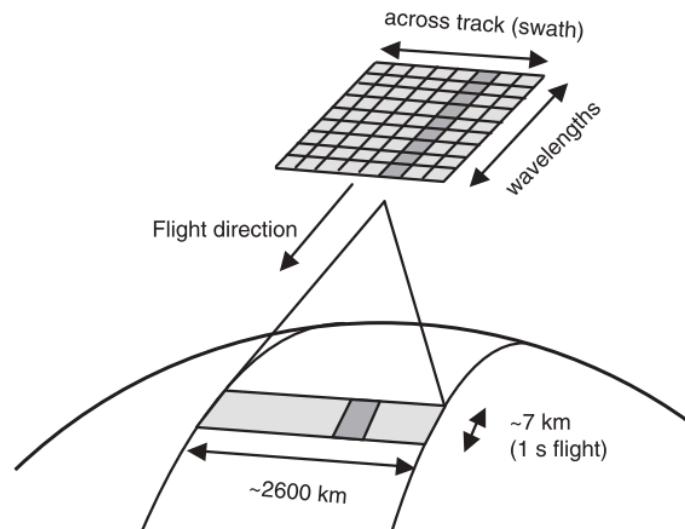


Figure 2.2: TROPOMI measurement principle: The instrument functions in a push-broom setup, covering a swath width of around 2,600 km on the Earth's surface. It has a nadir spatial resolution of $7 \times 7 \text{ km}^2$ for carbon monoxide (CO) and $3.5 \times 7 \text{ km}^2$ for nitrogen dioxide (NO_2). This figure has been taken from Veefkind et al. [18].

interest) [31]. In this study, the NO_2 column density is expressed in units of millimoles per square metre (mmol/m^2).

Carbon monoxide (CO)

Due to its ability to detect changes in carbon monoxide (CO) concentrations in the lower troposphere, the TROPOMI Short Wave Infrared (SWIR) measurements are well suited for correlating satellite CO observations with emission sources. The TROPOMI radiance measurements in the SWIR range, specifically between 2305 and 2385 nm, show absorption characteristics related to CO. The CO column density is observed globally on a daily basis with a spatial resolution of $7 \times 7 \text{ km}^2$ in nadir. However, the ground pixel resolution was enhanced to $7 \times 5.5 \text{ km}^2$ from the 6th of August, 2019 [32]. The Shortwave Infrared Carbon Monoxide Retrieval algorithm (SICOR) is employed to convert spectral radiances into CO column densities [33]. Biases are well within the mission requirement of maximum bias equal to 15% (see Table 2.1). As a user guideline for the data quality, a quality assurance value is given with the data. It is recommended to only use those pixels with a quality assurance value of above 0.5 [31]. In this study, the CO column density is expressed in units of moles per square metre (mol/m^2).

The TROPOMI retrievals of NO_2 and CO used in this study are averaged over a 5×5 pixel grid surrounding the fire locations. This approach, used by [21], addresses the issue of diffused information and is particularly crucial for NO_2 , which can exhibit erratic behaviour in smaller pixels.

Table 2.1: NO_2 and CO data product requirement

Parameter	Data Product	Vertical Resolution	Bias
NO_2	Stratospheric NO_2	Stratospheric column	< 10%
NO_2	Tropospheric NO_2	Tropospheric column	25-50%
Total column	Carbon monoxide (CO)	Total column	15%

Super-observations

The spatial resolution of satellite data is significantly finer than that of model grids. To bridge these spatial scale gaps, [25] provides a framework for generating more reliable and representative data for data assimilation purposes in models which is called the super-observation approach. In this approach,

a weighted average method is used to obtain super-observations. A super-observation is created by averaging all data within a specific grid cell designated for super-observation (see Equation 2.2). The weighting factor for individual data is estimated based on the coverage area by individual data pixels and the total coverage area for a super-observation grid.

$$\bar{y} = \frac{\sum_{l=1}^m w_l y_l}{\sum_{l=1}^m w_l} \quad (2.2)$$

where \bar{y} represents the concentration of a super-observation, derived from multiple individual data concentrations y_l ; m represents the quantity of observations within a super-observation grid; w_l is a weighting factor calculated as the ratio of the coverage area of an individual data point to the total coverage area of all data used to generate the super-observation grid. This means that data points with greater coverage are assigned higher weighting factors reflecting greater reliability.

In this study, TROPOMI retrievals are regridded at four different resolutions of $0.5^\circ \times 0.5^\circ$, $0.4^\circ \times 0.4^\circ$, $0.3^\circ \times 0.3^\circ$ and $0.25^\circ \times 0.25^\circ$ using the super observation approach. A resolution coarser than $0.5^\circ \times 0.5^\circ$ could experience loss of information while finer than $0.25^\circ \times 0.25^\circ$ would be close to the retrieval resolution and not much difference is expected in the results. Therefore, this study limits the choice of resolution to between $0.5^\circ \times 0.5^\circ$ and $0.25^\circ \times 0.25^\circ$.

2.2.2. Environmental Indicators

Standard Precipitation-Evapotranspiration Index (SPEI)

The Standard Precipitation-Evapotranspiration Index (SPEI) is a multi scalar drought index that uses precipitation and potential evapotranspiration (PET) to determine drought. In this study, SPEIbase v2.0, derived from the FAO-56 Penman-Monteith method for estimating PET is used [34]. The difference between the precipitation (P) and PET for the month i is calculated (see Equation 2.3) which offers a straightforward measure of the water surplus or deficit (D) for the analysed month.

$$D_i = P_i - PET_i \quad (2.3)$$

The Global SPEI database, SPEIbase provides extensive data on drought conditions at the global scale with a spatial resolution of $0.5^\circ \times 0.5^\circ$ and a monthly temporal resolution. The SPEI can account for the possible effects of temperature extremes such as heat waves therefore is better than other drought indexes such as self-calibrated Palmer drought severity index (sc-PDSI) and standardised precipitation index (SPI) [34]. The multi-scalar aspect of the SPEI allows for the recognition of various types of drought and their impacts on different systems. The method for computing the SPEI is similar to that of the SPI. However, the SPEI utilises the "climatic water balance," which is the difference between precipitation and reference evapotranspiration, instead of just precipitation. This climatic water balance compares the present water with the atmospheric evaporative demand, thereby offering a more dependable gauge of drought severity than solely relying on precipitation. The study by [34], therefore recommends the use of SPEI in preference to the sc-PDSI. The SPEI enables the evaluation of drought severity across different time spans (i.e. over one month, two months, three months, etc.), which is crucial for understanding the diverse reactions to drought across various hydrological, environmental, and socioeconomic systems [35]. The SPEI category classification is shown in Table 2.2.

Table 2.2: Agnew's classification scheme for drought categories [36]

SPEI values	Drought category
> 0	No drought
0 to -0.5	No drought
-0.5 to -0.84	Moderate drought
-0.84 to -1.28	Severe drought
-1.28 to -1.65	Extreme drought
< -1.65	Very extreme drought

Soil Moisture (SM)

Global satellite-based surface soil moisture observations were acquired from the Copernicus Climate Change Service (C3S) surface soil moisture (SSM) product version 202012. C3S SSM is a combined

dataset that integrates SSM retrievals from 4 active and 10 passive microwave sensors. It contains soil moisture estimates at a global scale at a daily, 10-day and monthly temporal resolution. Monthly data has been used in this study to keep it consistent with the SPEI dataset which is available at a monthly temporal resolution. They provide information regarding the top few centimetres of soil with a spatial resolution of $0.25^\circ \times 0.25^\circ$ [37]. Surface soil moisture is described as content of liquid water in a surface soil layer of 2 to 5 centimetre depth expressed as the percentage of total saturation.

The C3S soil moisture data can be accessed easily through the Copernicus Climate Data Store (CDS), and comprehensive details about the C3S dataset and its underlying European Space Agency's Climate Change Initiative (ESA CCI) v5 merging algorithm are available in the relevant documentation [37]. The uncertainty estimates associated with the combined surface soil moisture (SSM) retrievals in the C3S SSM product were determined using triple collocation analysis (TCA). In this approach, individual (stationary) uncertainties were initially assessed for each satellite sensor independently to derive merging weights. Subsequently, uncertainties in the merged SSM estimates were computed based on the law governing the propagation of uncertainties [38].

2.2.3. Land Cover Data

Global Fire Emission Database (GFED)

The Global Fire Emission Database version 4s (GFED4s), described in [39], provides global estimates of monthly burnt area, monthly emissions and fractional contributions of different fire types in order to calculate trace gas and aerosol emissions using emission factors. GFED uses the Carnegie–Ames–Stanford Approach (CASA) biogeochemical model. Input data includes burned area information from MODIS, and land cover maps sourced from the annual MODIS MCD12C1 land cover type product, using the University of Maryland (UMD) classification scheme [17]. Data is available at a spatial resolution of $0.25^\circ \times 0.25^\circ$. Compared to the previous version, GFED4s includes algorithm to account for small fires which enhance the overall burned area estimation, hence the inclusion of the "s" in the name. Emissions data are available for various substances including carbon (C), dry matter (DM), carbon dioxide (CO₂), carbon monoxide (CO), methane (CH₄), hydrogen (H₂), nitrous oxide (N₂O), nitrogen oxides (NO_x), non-methane hydrocarbons (NMHC), organic carbon (OC), black carbon (BC), particulate matter less than 2.5 microns (PM_{2.5}), total particulate matter (TPM), sulphur dioxide (SO₂) and others.

The emissions data files includes the contribution of fire sources to monthly-biomass-burning-dry-matter emissions which have been used in this study. Fire sources include savanna, grassland and shrubland (SAVA), boreal forest (BORF), temperate forest (TEMF), deforestation and degradation of the forests (DEFO), peat land (PEAT) and agricultural waste burning (AGRI) as indicated in Table 2.3. The uncertainties in the dataset are considerable and challenging to measure [17]. The user guide mentions that over larger areas, uncertainties in GFED emissions are expected to be around 50 %, but these uncertainties increase for smaller areas, particularly in regions where peatlands or deforestation significantly contribute to fire emissions.

Table 2.3: GFED Land Cover Classification System (GFED4s)

Name	Description
SAVA	Savanna, grassland, and shrubland fires
BORF	Boreal forest fires
TEMF	Temperature forest fires
DEFO	Tropical forest fires [deforestation and degradation]
PEAT	Peat fires
AGRI	Agricultural waste burning

Moderate Resolution Imaging Spectroradiometer (MODIS)

The MODIS Land Cover Type Product (MCD12Q1) Version 6.1, described in [40] is used in the study which provides worldwide land cover maps on an annual basis with a spatial resolution of 500 metres, covering the period from 2001 to the present day. This dataset is created by analysing MODIS Terra and Aqua reflectance data through supervised classifications. These classifications utilise various schemes including the International Geosphere-Biosphere Programme (IGBP), University of Maryland (UMD), Leaf Area Index (LAI), BIOME-Biogeochemical Cycles (BGC), and Plant Functional Types (PFT) to

identify different land cover types. Following this initial classification, further refinement of specific classes is achieved through additional post-processing techniques that integrate prior knowledge and supplementary information. The dataset also includes assessment layers for land cover properties based on the Food and Agriculture Organization (FAO) Land Cover Classification System (LCCS), which covers aspects such as land cover, land use, and surface hydrology. The product contains 13 Science Data Sets (SDS) out of which the Food and Agricultural Organisation (FAO)-Land Cover Classification System (LCCS1) is used in the study. It identifies 17 types of vegetation, 8 of which are found in the region of study and are shown in Table 2.4.

The estimated global accuracy of the International Geosphere-Biosphere Programme (IGBP) layer within the MODIS Collection 6 Land Cover Type product (MCD12Q1) is approximately 73.6 %. The dataset exhibits certain limitations and uncertainties. For instance, wetlands are not adequately represented. Certain grassland areas are categorised as savannas. Regions characterised by temperate evergreen needleleaf forests are incorrectly classified as broadleaf evergreen forests in Japan, the Pacific Northwest of North America, and Chile. Likewise, areas featuring evergreen broadleaf forests are misclassified as evergreen needleleaf forests in Australia and parts of South America. Additionally, in tropical regions where cropland field sizes are typically smaller than a MODIS pixel, agricultural areas are occasionally underrepresented [40].

Table 2.4: FAO Land Cover Classification System (LCCS1). It has a total 17 classes of land use type. However, only those found in the region of study are shown here.

Name	Description
Evergreen Needleleaf Forests	Dominated by evergreen conifer trees (>2m). Tree cover >60%.
Mixed Broadleaf/Needleleaf Forests	Co-dominated (40-60%) by broadleaf deciduous and evergreen needleleaf trees (>2m). Tree cover >60%.
Open Forests	Tree cover 30-60% (canopy >2m).
Sparse Forests	Tree cover 10-30% (canopy >2m).
Dense Herbaceous	Dominated by herbaceous annuals (<2m) with at least 60% cover.
Sparse Herbaceous	Dominated by herbaceous annuals (<2m) with 10-60% cover.
Shrubland/Grassland Mosaics	Dominated by woody perennials (1-2m) with 10-60% cover and dense herbaceous annual understory.
Barren	At least 60% of the area is non-vegetated barren (sand, rock, soil) or permanent snow/ice with less than 10% vegetation.

2.2.4. Moderate Resolution Imaging Spectroradiometer (MODIS) active fire product

Fires are analysed with MODIS aboard the Terra and Aqua satellites. The MODIS Thermal Anomalies/Fire Daily L3 Global Product MOD14A2 (Terra) and MYD14A2 (Aqua) at 1 km spatial resolution is used to find fire locations. Fire detection is accomplished using a contextual algorithm [41] that utilises the intense emission of mid-infrared radiation emitted by fires [42], [43]. This algorithm analyses every pixel within the MODIS swath and categorises each into one of the following classes: missing data, cloud, water, non-fire, fire, or unknown. Validation of the Terra MODIS active fire product has mainly been carried out using concurrent, detailed fire maps generated from Advanced Spaceborne Thermal Emission and Reflection Radiometer (ASTER) imagery. Given that the accuracy of fire hotspot locations is limited to 1 km when relying on MODIS active fire data, having land use information at an extremely detailed resolution of approximately 10 meters as provided by ESA WorldCover may not be as crucial. Hence, for this investigation, the MODIS Terra+Aqua Combined Land Cover product, available at a resolution of 500 metres is used since it reasonably matches the spatial resolution of active fire locations.

The locations of these fires are used in other datasets to determine relevant quantities such as

column concentrations of NO₂ and CO, SPEI, SM and vegetation type. There was no fire detected in the southern region on the 10th of September, 2020. According to the product user guide, several reasons could lead to such a situation. The fire might have ignited and extinguished between satellite passes. It could be too small or too cool to be detected within the 1 km² MODIS footprint. Additionally, cloud cover, dense smoke or tree canopy might completely conceal the fire. Therefore, this particular date has been excluded from the study.

2.2.5. ERA5 Wind

ERA5 is the fifth generation European Centre for Medium-Range Weather Forecasts (ECMWF) reanalysis providing global climate and weather data. It provides hourly estimates for a large number of atmospheric, ocean-wave and land-surface quantities which are available at a resolution of 0.25°×0.25° [44]. For this study, hourly, 10 metre wind components data is used to determine appropriate background location for sampling NO₂ and CO to prevent contamination from other sources.

3

Results

3.1. Mole Density Ratio

Scatter plots from the study of [21] have been reproduced as Figure 3.1 to provide a basis for comparison with similar scatter plots created using super-observation data at different resolutions. Each subplot represents a different time period of approximately 10 days, showing the relationship between enhancements (relative to the background) of nitrogen dioxide (ΔNO_2) and carbon monoxide (ΔCO) over time for fire hotspots in the northern and southern regions. The first period is the initiation of the fire where most fire hotspots are concentrated at lower values of ΔNO_2 and ΔCO . The northern region witnesses rapid spread of fire in the second period indicated by increase in the number of coloured markers which represent fire hotspots. The markers are now more spread showing higher enhancement values. For the southern region, this spread of fire continues upto the third period. In the subsequent periods, the fires in both regions gradually diminish, as indicated by the reduced number of coloured markers. By the final period, the data points are tightly clustered at lower enhancement values which show that the number of fire hotspots has significantly decreased accompanied by reduction in enhancements values, indicating the diminishing phase of wildfires. In the northern region, the average Mole Density Ratio (MDR) values start at 0.52, increases in early September, then decreases, peaks again at the end of September, and finally decreases to 0.43 in October. In the southern region, the range of MDR is higher than in the north. It starts at high value of 2.68 in late August, decreases significantly in early September, then follows a more stable pattern with slight fluctuations through the subsequent periods, finally reaching a value of 0.71 in October (see Figure 3.1). The reasons for such variations within a region and between the two regions are explained in the subsequent sections.

Similar scatter plots are created using super-observations at different spatial resolutions (see Figure 3.2 - Figure 3.5). These scatter plots using super-observations revealed different MDR values when compared to MDR values obtained using data at TROPOMI resolution. For instance, MDR estimated using super-observations at a spatial resolution of $0.25^\circ \times 0.25^\circ$ (see Figure 3.2), showcase relatively minor differences in the northern region. In contrast, the southern region displayed much more significant differences. Throughout the observed periods, the southern region consistently showed lower MDR values than the MDR values estimated using data at TROPOMI resolution. However, there was a notable exception in the final period, during which the MDR value increased rather than decreased, deviating from the previously observed trend.

The resolution of $0.3^\circ \times 0.3^\circ$ shows MDR values similar to those of the $0.25^\circ \times 0.25^\circ$ resolution, except for the last period in the southern region where the difference is more than 1.0. The MDR values obtained at the resolution of $0.4^\circ \times 0.4^\circ$ are similar to those of TROPOMI resolution in the northern region but they differ significantly in the southern region. Both the $0.4^\circ \times 0.4^\circ$ and $0.5^\circ \times 0.5^\circ$ resolutions exhibit the lowest MDR values among all resolutions.

Several enhancements were observed to be zero in the southern region, where a distance of 30 km upwind is used to sample background, potentially due to sampling of NO_2 and CO from the same grid cell as the fire. This issue was particularly pronounced at coarser resolutions (see Figure A.1), resulting in a reduction in the data points available to calculate MDR.

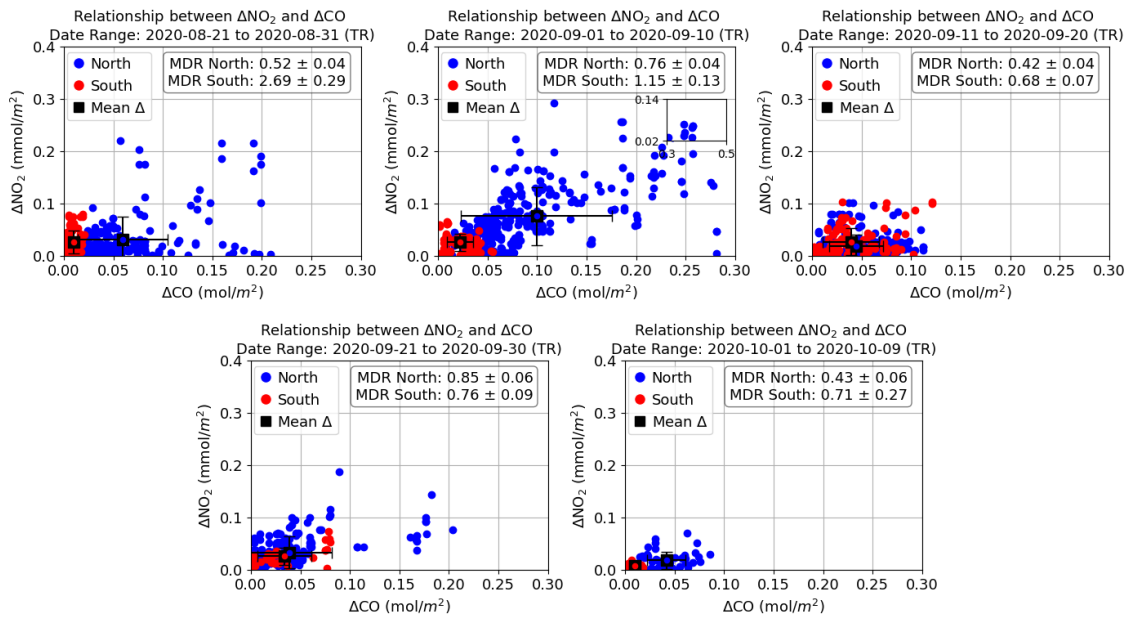


Figure 3.1: Relationship between ΔNO_2 and ΔCO over various periods of the wildfire in the northern and southern regions for data at TROPOMI Resolution (TR). The legend includes the average MDR for each period considered along with the standard deviation values. The inset plot indicates the outliers. The black square box with error bars represent the mean of ΔNO_2 and ΔCO and their standard deviation values.

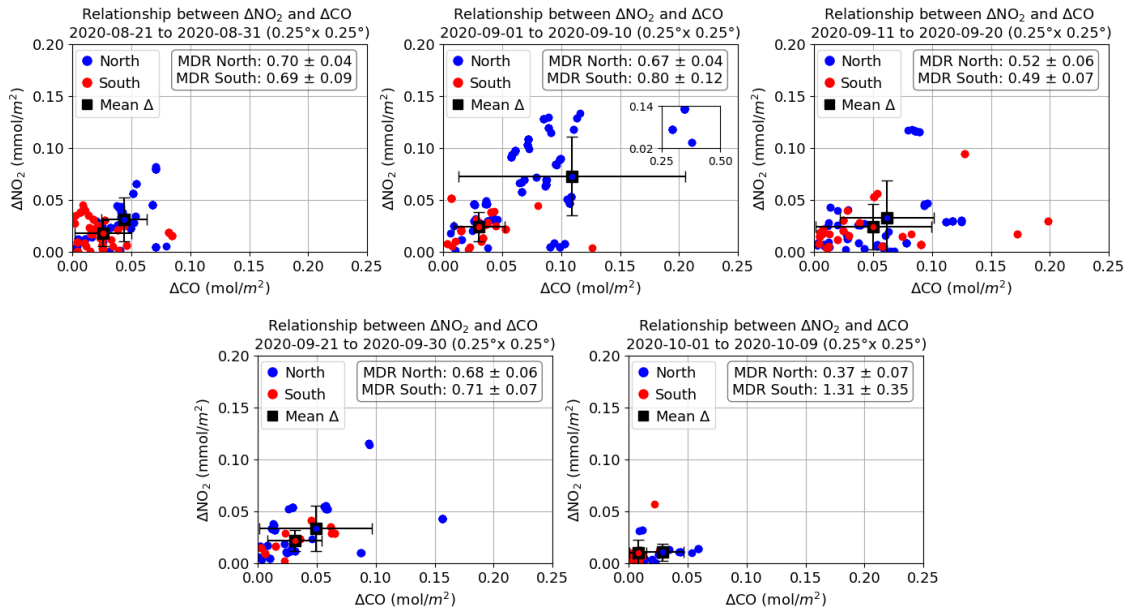


Figure 3.2: Relationship between ΔNO_2 and ΔCO over various periods of the wildfire in the northern and southern regions for the first set of super observation data at a resolution of $0.25^\circ \times 0.25^\circ$. The legend includes the average MDR for each period considered along with the standard deviation values. The inset plot indicates the outliers. The black square box with error bars represent the mean of ΔNO_2 and ΔCO and their standard deviation values.

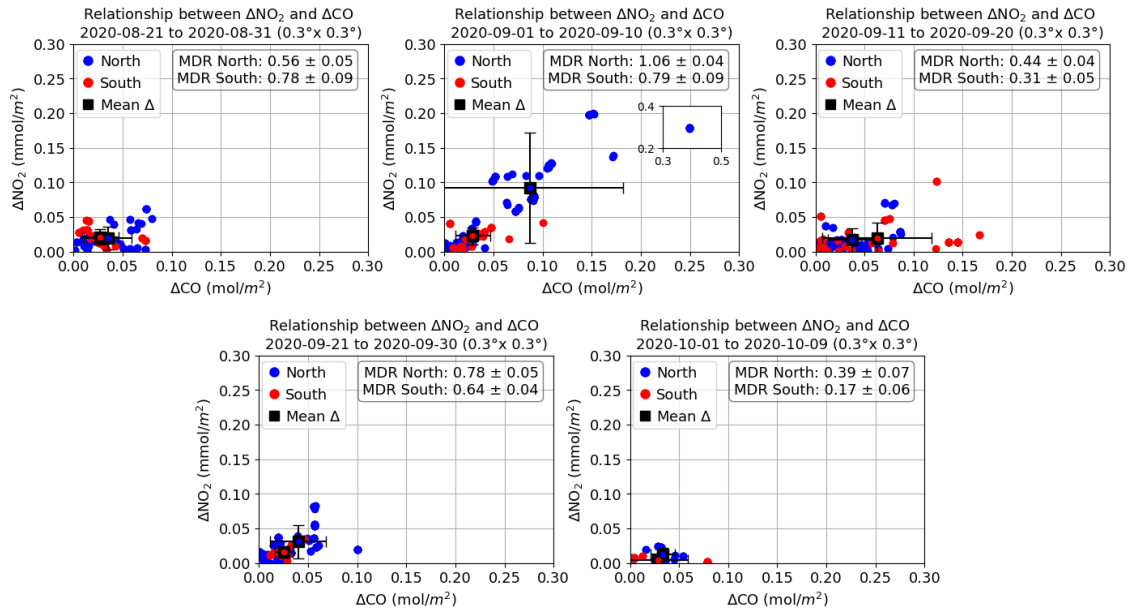


Figure 3.3: Relationship between ΔNO_2 and ΔCO over various periods of the wildfire in the northern and southern regions for the second set of super observation data at a resolution of $0.3^\circ \times 0.3^\circ$. The legend includes the average MDR for each period considered along with the standard deviation values. The inset plot indicates the outliers. The black square box with error bars represent the mean of ΔNO_2 and ΔCO and their standard deviation values.

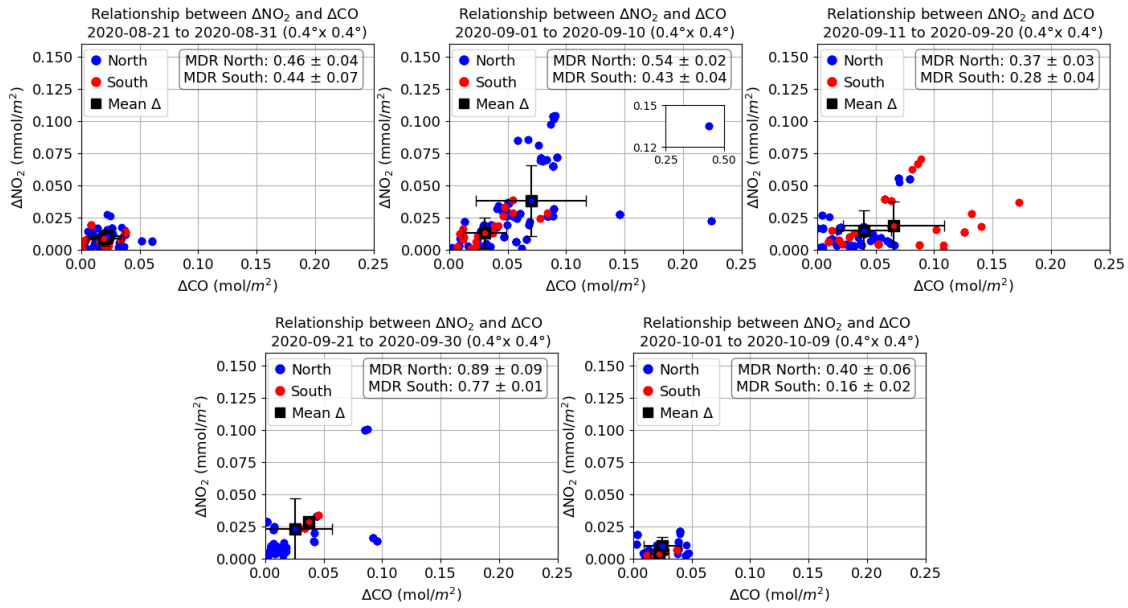


Figure 3.4: Relationship between ΔNO_2 and ΔCO over various periods of the wildfire in the northern and southern regions for the third set of super observation data at a resolution of $0.4^\circ \times 0.4^\circ$. The legend includes the average MDR for each period considered along with the standard deviation values. The inset plot indicates the outliers. The black square box with error bars represent the mean of ΔNO_2 and ΔCO and their standard deviation values.

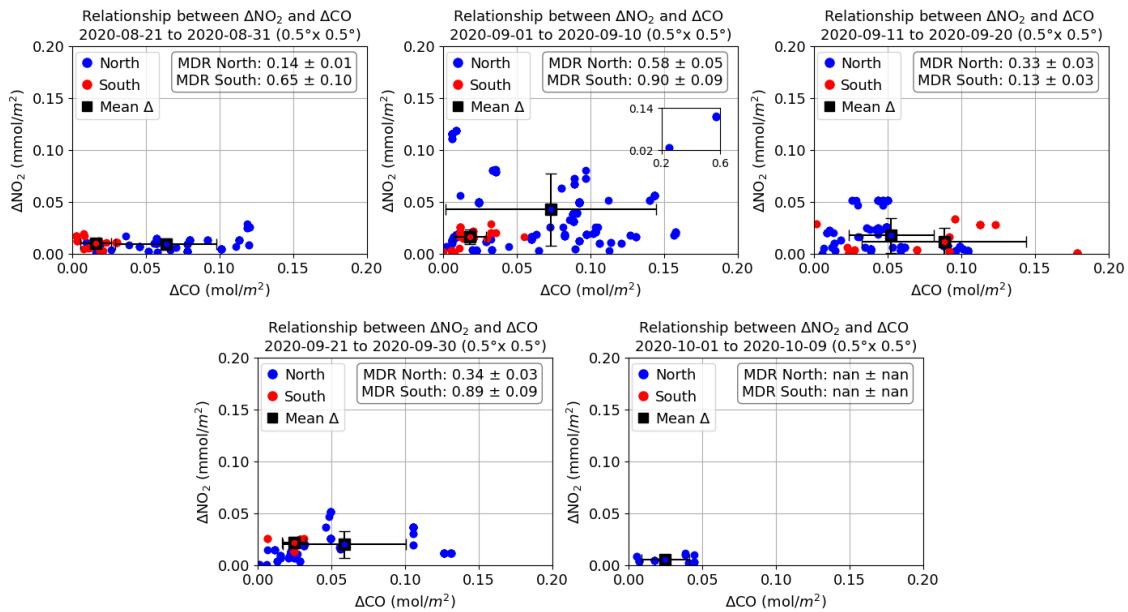


Figure 3.5: Relationship between ΔNO_2 and ΔCO over various periods of the wildfire in the northern and southern regions for the fourth set of super observation data at a resolution of $0.5^\circ \times 0.5^\circ$. The legend includes the average MDR for each period considered along with the standard deviation values. The inset plot indicates the outliers. The black square box with error bars represent the mean of ΔNO_2 and ΔCO and their standard deviation values. The estimated average MDR in the final period is nan due to insufficient number of data points while sampling enhancements using Monte Carlo simulation.

The MDR values estimated using datasets at TROPOMI resolution and different super-observation resolutions have been summarised in Figure 3.6 for both the northern the southern region.

In the northern region, the temporal trend of MDR across various fire periods remains largely consistent across all resolutions examined. Specifically, the MDR values show an increase from the first to the second period, followed by a decrease from the second to the third period. This pattern continues with an increase from the third to the fourth period, and then a subsequent decrease from the fourth to the fifth period. The discrepancies in MDR estimates across different resolutions during the third and fifth periods are relatively minor. However, during the other periods, these discrepancies appear to be considerably more pronounced (see Figure 3.6).

In the southern region, the temporal trend of MDR remains largely consistent across all resolutions examined during the second, third, and fourth periods. Specifically, MDR values decrease from the second to the third period and then increase from the third to the fourth period. The variations in MDR estimates across different resolutions during the fourth period are relatively minor. However, in other periods, these variations are significantly more pronounced, indicating greater discrepancies (see Figure 3.6). For instance, in the first period, the difference in MDR estimation when using super-observations compared to data at TROPOMI resolution is approximately 2.0, which is quite substantial. Similar differences are observed during other periods as well, although these discrepancies are somewhat smaller.

A comparison of these MDR values across different resolutions suggests that there is considerable discrepancy in MDR estimates when super-observations at the specified resolutions are used. The temporal variations in MDR estimations are explained in detail in section 3.3.

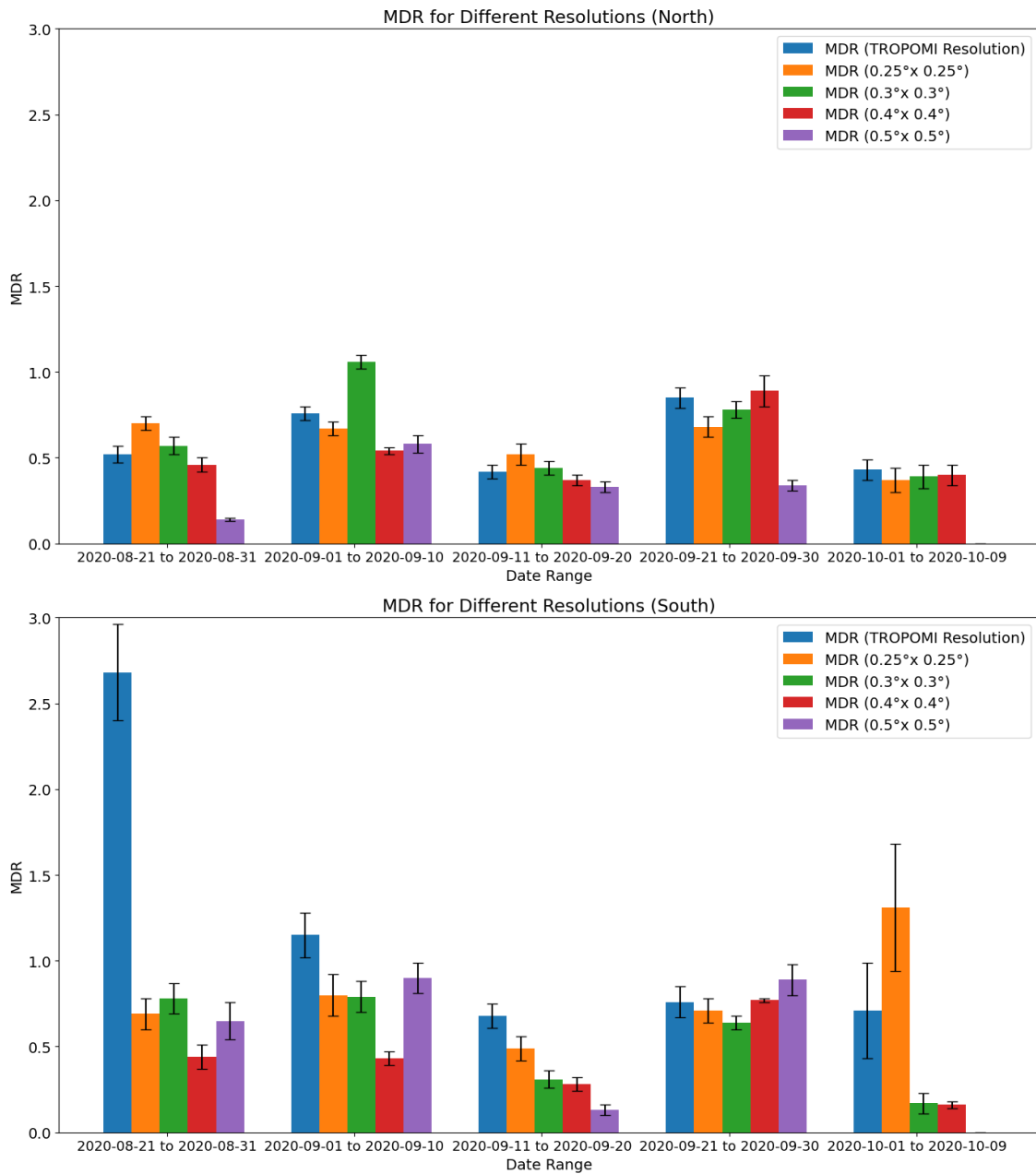


Figure 3.6: The bar chart provided shows the variation of MDR values for datasets at different resolutions over various date ranges through the fire period in the northern (top) and southern region (bottom). Each bar represents the MDR value for a specific resolution within a particular date range. Each date range has multiple bars, each coloured differently to represent different resolutions. The error bars on top of each bar are standard deviation values, which indicate the uncertainty in the MDR values. The MDR for $0.5^{\circ} \times 0.5^{\circ}$ is absent in the last period due to insufficient number of data points while sampling enhancements using Monte Carlo simulation.

3.2. Mole Density Ratio (MDR) and Environmental Indicators

This section provides an analysis of the influence of environmental indicators, such as drought conditions and soil moisture levels, on MDR based on TROPOMI resolution. By examining the interplay between these environmental indicators and MDR, this analysis aims to discover any significant correlations between them.

3.2.1. MDR link with Standard Precipitation-Evapotranspiration Index (SPEI)

To investigate the effect of drought conditions on MDR, an analysis was conducted on the changes in the Standard Precipitation-Evapotranspiration Index (SPEI) through the fire periods. Additionally, the change in average Mole Density Ratio (MDR) for these periods, calculated in section 3.1, was compared to change in SPEI values to explore any potential correlations between MDR and drought conditions (see Figure 3.7).

In the northern region, the initial conditions were characterised by dryness, indicated by an SPEI value of -1.4. Although conditions showed some improvement during the subsequent periods, a deterioration was observed by the end of the wildfire, with the SPEI value dropping further to -1.6.

A similar trend was noted in the southern region. Initially, drought conditions improved, with the SPEI value increasing from -0.6 in the first period to -0.4 during the intermediate periods. However, the situation worsened towards the end of the wildfire, with the SPEI reaching a value of -1.0.

The spatial distribution of the wildfire in the northern region ($\approx 1^\circ \times 1^\circ$) was more dispersed compared to the southern region ($\approx 0.5^\circ \times 0.5^\circ$) as visible in the satellite images (see Figure 1.3 and Figure 1.4). This dispersal could be a contributing factor to the greater variation in SPEI observed during the study period in the northern region. In contrast, the wildfire in the southern region had a more condensed spatial distribution. Additionally, the low spatial resolution of the SPEI database ($0.5^\circ \times 0.5^\circ$), might explain the relatively small variations observed in SPEI values. Moreover, as the SPEI database are monthly averages, SPEI values seem to remain consistent within the same month across different fire periods in the southern region.

Furthermore, it is noted that changes in MDR did not show a consistent pattern corresponding to changes in SPEI (see Figure 3.7). This lack of consistency suggests that there is no clear or direct relationship between drought conditions, as measured by SPEI, and the average MDR. Consequently, it can be concluded that the link between drought conditions and MDR is not evident from the data analysed.

However, vegetation responses to drought conditions vary among different vegetation types. For instance, grasslands may be more sensitive to short-term droughts, whereas forests are likely to be more affected by prolonged drought periods [45]. Not accounting for this variation in sensitivity among different vegetation types could introduce a source of uncertainty in the analysis.

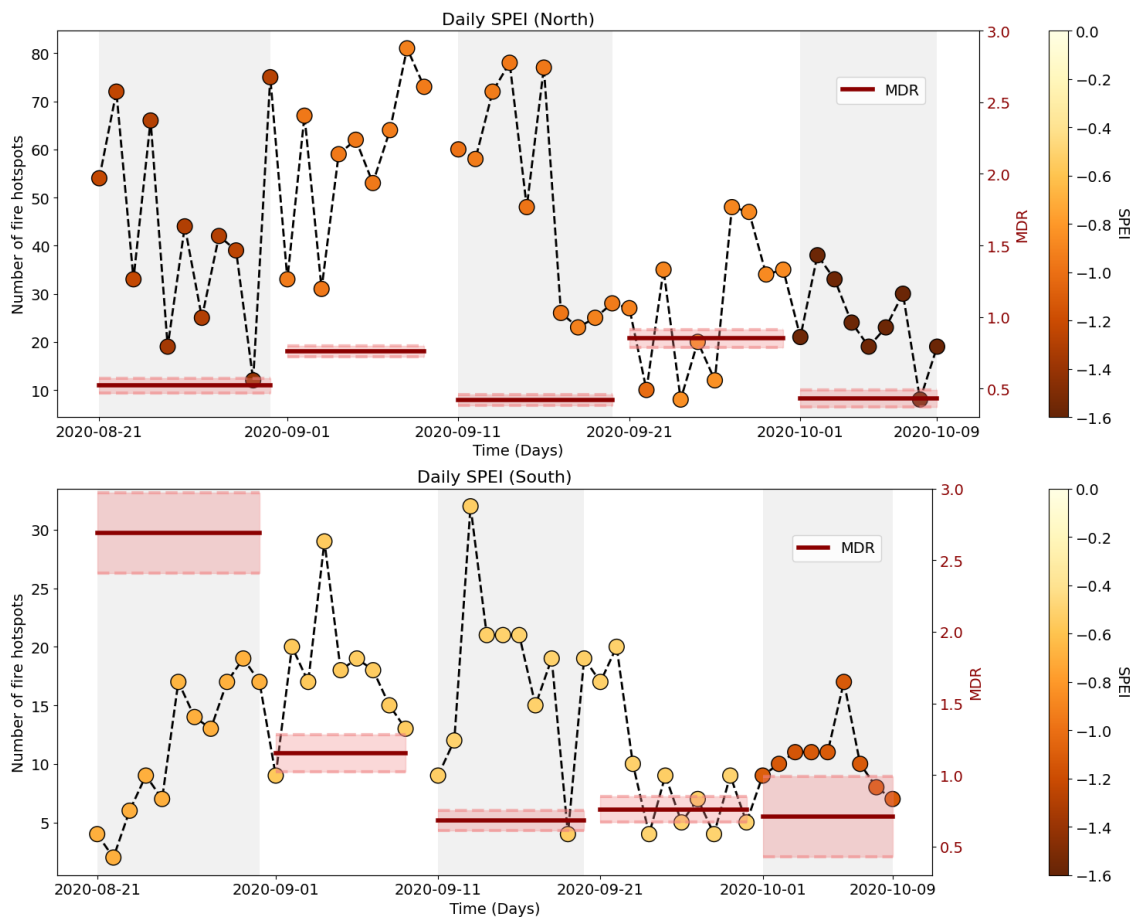


Figure 3.7: Time series illustrating the variation in Standard Precipitation-Evapotranspiration Index (SPEI) values alongside corresponding changes in the average Mole Density Ratio (MDR) in both northern and southern regions. The circular coloured markers represent SPEI values while the red horizontal bars indicate average MDR values measured on the right Y-axis. The shaded region is the standard deviation values of the MDR. The left Y-axis represents the number of fire hotspots, while the X-axis indicates the number of days. A high negative SPEI value indicates a more intense drought condition.

3.2.2. MDR link with Soil Moisture (SM)

Similar to the investigation of the effect of drought conditions on MDR, an analysis was also conducted on the changes in soil moisture (SM) content across various wildfire periods and its potential correlation to MDR (see Figure 3.8). In the northern region, the SM values commence at 30 % during the first fire period. These values increase to 40 % in the second period, followed by a slight decrease to 35 % in the third period. The fourth period witnesses a marginal increase in SM values, with a further rise reaching up to 40 % during the final period, marking the end of the fire.

In the southern region, initially, the SM values range between 40 % and 50 %. These values rise to approximately 60 % during the second period, followed by a slight dip in the third period. Subsequently, there is a rise in the SM values in the following periods, ultimately reaching up to 65 % during the final period. The southern region witnesses greater variation and higher values of SM content compared to the northern region. This could be attributed to the presence of several water bodies and a more dynamic topography in the southern region; however, the overall trend remains similar to that observed in the northern region.

Consequently, as evident from Figure 3.8, there is no clear or consistent relationship between the changes in SM values and the variations in average MDR. Despite the observed fluctuations in soil moisture across different periods and regions, these changes do not correspond to any detectable pattern in MDR.

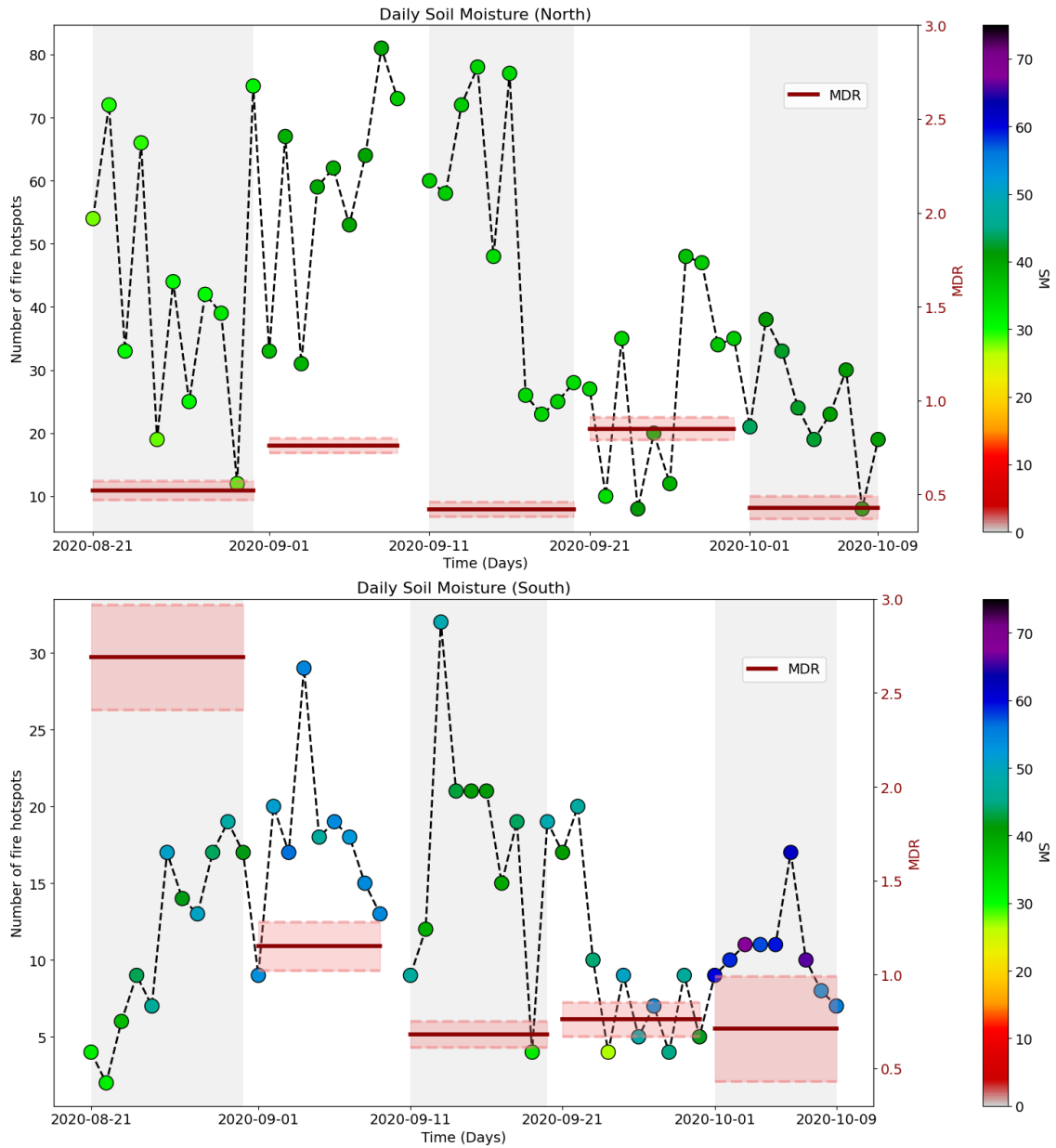


Figure 3.8: Time series illustrating the variation in soil moisture (SM) values alongside corresponding changes in the average Mole Density Ratio (MDR) in both northern and southern regions. The circular coloured markers represent SM values while the red horizontal bars indicate average MDR values measured on the right Y-axis. The shaded region is the standard deviation values of the MDR. The left Y-axis represents the number of fire hotspots, while the X-axis indicates the number of days. SM values are in percentage.

3.3. Mole Density Ratio (MDR) and Land Cover

This section provides an analysis of the influence of various types of vegetation on MDR, based on two distinct land use datasets: Global Fire Emission Database (GFED) and Moderate Resolution Imaging Spectroradiometer (MODIS). The analysis explores how different vegetation categories, as classified by these datasets, affect estimation of MDR based on TROPOMI resolution. By comparing the impacts of different vegetation types, it aims to identify significant patterns and correlations that contribute to variations in MDR.

3.3.1. MDR link with GFED Land Cover

In the northern region, temperate forests dominate throughout the period, consistently making up the majority of the vegetation cover while savanna, grassland, and shrubland are present sporadically and shows some variation over time. Agricultural waste is relatively small and more or less has a constant percentage throughout the period. The MDR values remain quite low, typically under 1.0. The last period where temperate forest is almost the sole vegetation type corresponds to one of the lowest MDR values (see Figure 3.9). However, the small variations in MDR observed from a period to another are likely not due to changes in vegetation, as the region maintains a fairly constant vegetation type. The presence of winds could have played a role in these variations as suggested by [21]. Strong winds occurred during the second period in the northern region (see section A.3). Windy conditions promote flaming type of combustion [19], which could explain the increase in MDR from the first to the second period. The subsequent minor changes in MDR could also be attributed to change in wind conditions.

For the southern region, the variation in vegetation is more prominent. In this region, savanna, grassland, and shrubland predominates throughout the period, making up the majority of the vegetation cover while temperate forests are present intermittently with noticeable fluctuations over time. Agricultural waste appears occasionally with a more or less constant percentage through the period. The MDR values vary between 0.5 and 3.0, indicating considerable variation (see Figure 3.9). This variation in MDR is likely caused by the change in vegetation. The MDR value is high around 2.5 in the first period when dominant vegetation is savanna, grassland, and shrubland with a bit of agricultural waste. It significantly decreases during the second and third periods, aligning with an increase in the percentage of temperate forests. This drop in MDR is due to the fire shifting to Sequoia National Park (SNP), an area dominated by forests, which causes a transition from flaming to smouldering combustion. These findings are consistent with the results of [21], which show that savanna type of vegetation is linked to higher MDR and flaming combustion, while temperate forests type of vegetation are linked to lower MDR and smouldering combustion.

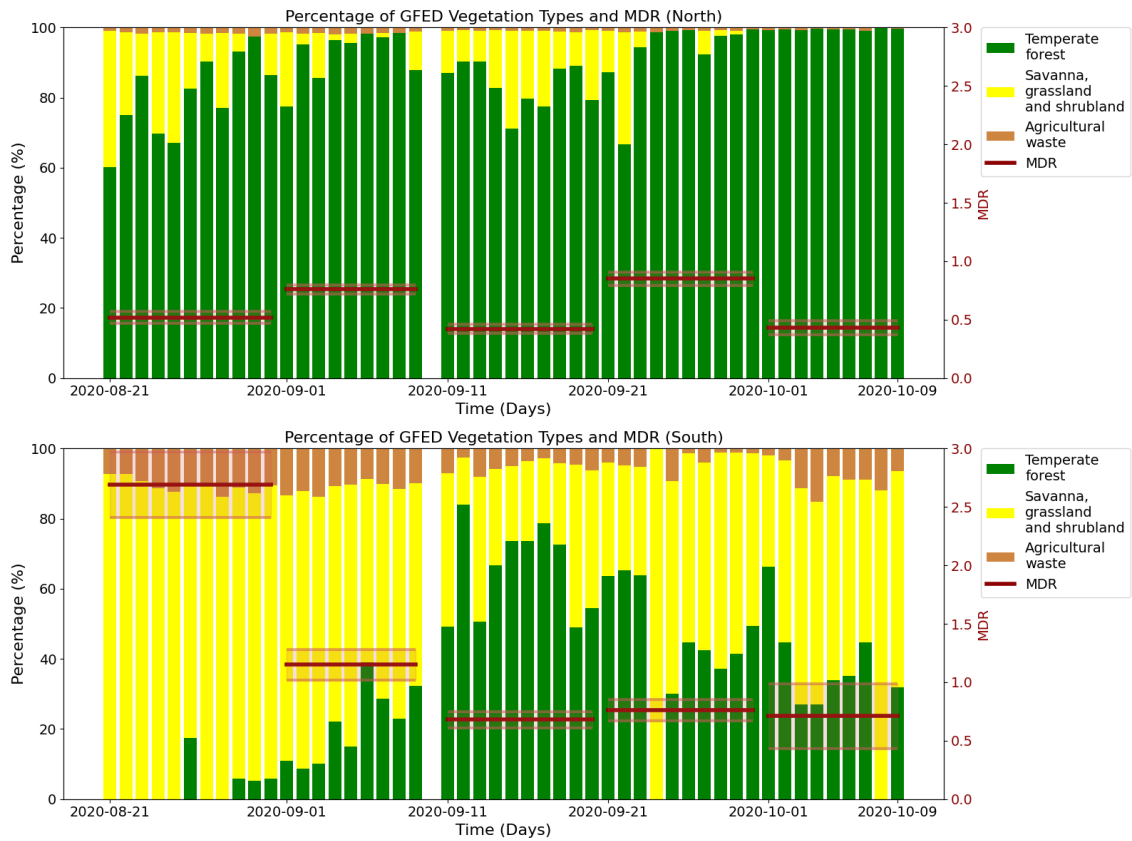


Figure 3.9: The image illustrates the percentage distribution of various GFED vegetation types alongside average MDR over specified fire periods in the northern and southern regions. The stacked bar chart shows the percentage of each vegetation type represented by various colours. Overlaid on this distribution, the red horizontal bars represent the average MDR values over the same period, measured on the right Y-axis. The shaded region indicates the standard deviation values of the estimated MDR showcasing uncertainty in the measurement.

3.3.2. MDR link with MODIS Land Cover

Figure 3.10 is a figure similar to Figure 3.9 but uses a much finer resolution MODIS land-use classification instead of GFED. A similar trend in vegetation change is indicated by both figures but Figure 3.10 gives us a more detailed information regarding the change in several vegetation type over the fire periods.

In the northern region, Evergreen Needleleaf Forests and Mixed Broadleaf/Needleleaf Forests dominate the vegetation cover, with a significant portion throughout the period. Open Forests and Dense Herbaceous also contribute significantly but vary more over time. Sparse Forests and Sparse Herbaceous are present in smaller proportions. The northern region shows a more stable MDR with less pronounced peaks. However, change in MDR could be attributed to change in vegetation to some extent unlike Figure 3.9 where it was difficult to correlate vegetation change to MDR. Between the first and second periods, there is a slight increase in MDR, which correlates with a reduction in Evergreen Needleleaf Forests and a consistent presence of Dense Herbaceous vegetation. From the second to the third period, the MDR declines, likely due to the emergence of Mixed Broadleaf/Needleleaf Forests and a minor decrease in Dense Herbaceous vegetation. Between the third and fourth periods, the MDR rises again, aligning with a decrease in Evergreen Needleleaf Forests. However, in the final period, the MDR drops, corresponding to an increase in Evergreen Needleleaf Forests and disappearance of Dense Herbaceous vegetation.

In the southern region, Open Forests and Sparse Forests are more prevalent, with Sparse Forests having a higher percentage than in the northern region. Dense Herbaceous and Sparse Herbaceous also have a significant presence, with noticeable variations over time whereas Barren is present sporadically in small percentages. The southern region exhibits more variability in MDR, indicating a more dynamic landscape. The significant dip in the MDR value up to the third fire period corresponds to decrease in percentage of Sparse Forests and dense herbaceous with an increase in percentage of Evergreen Needleleaf Forests and Open Forests. A similar relationship between MDR and vegetation type is seen in the last two fire periods where the MDR increases slightly before dipping again.

In both the regions, an increase in less dense vegetation types like Sparse Forests, Sparse Herbaceous and Barren tends to be associated with higher MDR values. Dense forest cover like Evergreen Needleleaf and Mixed Broadleaf/Needleleaf tends to be linked to lower MDR values. Similar to the results of subsection 3.3.1, this analysis is also in alignment with the study of [21], additionally providing a more detailed understanding of the effect of various vegetation types on MDR.

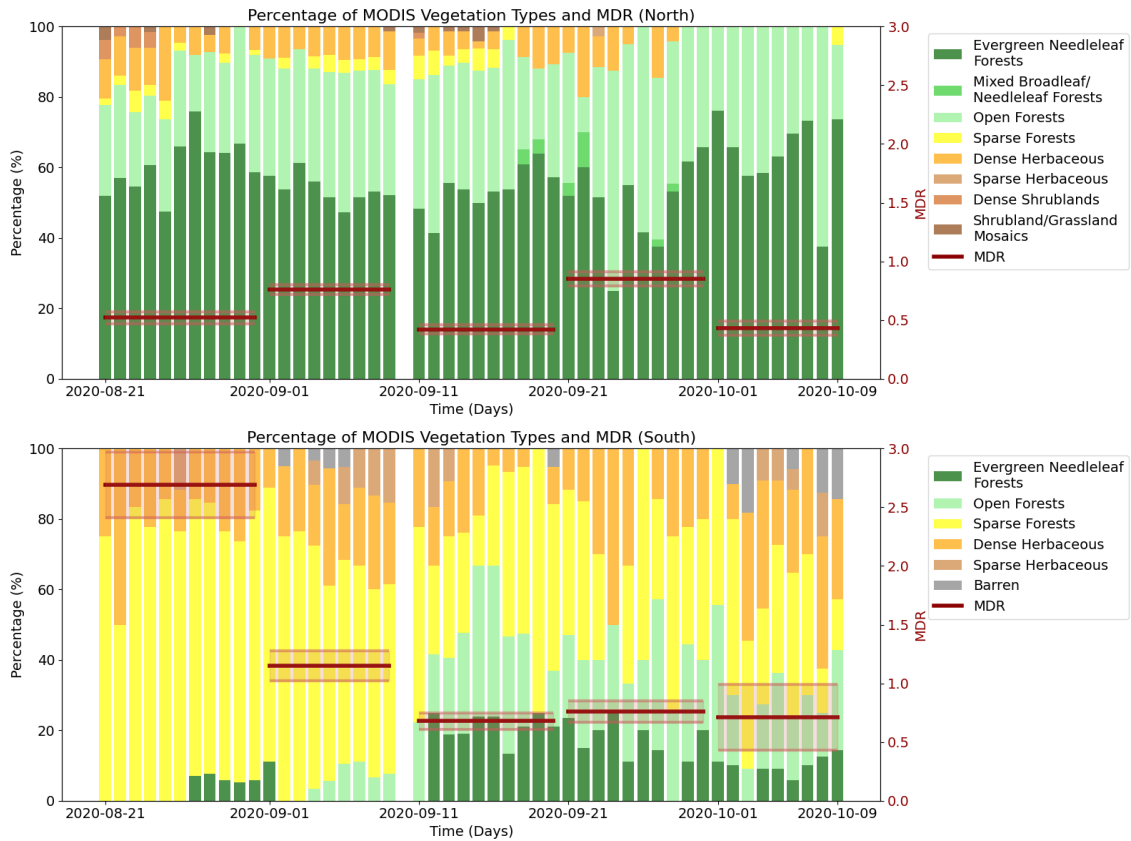


Figure 3.10: The image illustrates the percentage distribution of various MODIS vegetation types alongside average MDR over specified fire periods in the northern and southern regions. The stacked bar chart shows the percentage of each vegetation type represented by various colours. Overlaid on this distribution, the red horizontal bars represent the average MDR values over the same period, measured on the right Y-axis. The shaded region indicates the standard deviation values of the estimated MDR showcasing uncertainty in the measurement. Compared to Figure 3.9, this figure offers a more detailed analysis of the effect of vegetation on MDR due to the higher resolution data and a more extensive classification of vegetation types.

3.3.3. Daily MDR link with MODIS Land Cover

For this analysis, the daily average MDR values based on TROPOMI resolution were calculated instead of the 10-day average MDR used earlier, to determine if variations in daily average MDR could be correlated to changes in vegetation according to MODIS land use data (see Figure 3.11). The daily MDR shows fluctuations between values of approximately 0 and 8 for both the regions. These variations are less prominent in the northern region compared to the southern region which is also the case in 10-day average MDR due to the presence of more types of vegetation in the southern region. Higher MDR values often coincide with the low percentage of forest vegetation types and high percentage in less dense vegetation types like Sparse Forests and Sparse Herbaceous. Days with high coverage of dense type of vegetation (Evergreen Needleleaf) generally show lower MDR values. There are a few days where MDR could not be calculated due to unavailability of positive enhancements of NO₂ and CO. On certain days, the standard deviation values are 0 since only one enhancement data was available for that particular day. For instance, on the day of 24th of August, 2020 (in the northern region) only one positive enhancement data was available for MDR calculation. A data availability analysis was performed to identify the days with sufficient information to provide a reasonably accurate estimation of MDR (see Figure A.2).

Over the span of several days, fires can spread, leading a 10-day average to include a wider range of vegetation types. When analysing daily MDR, there tends to be less mixing of different regions into a single estimate. Therefore, the link between MDR and vegetation type is likely to be observed over shorter time intervals. This analysis suggests that there is a link between change in daily MDR and vegetation type, with denser and predominantly forest type of vegetation cover contributing to lower MDR values and vice versa. Therefore, some possibility exists to track daily MDR change with respect to vegetation.

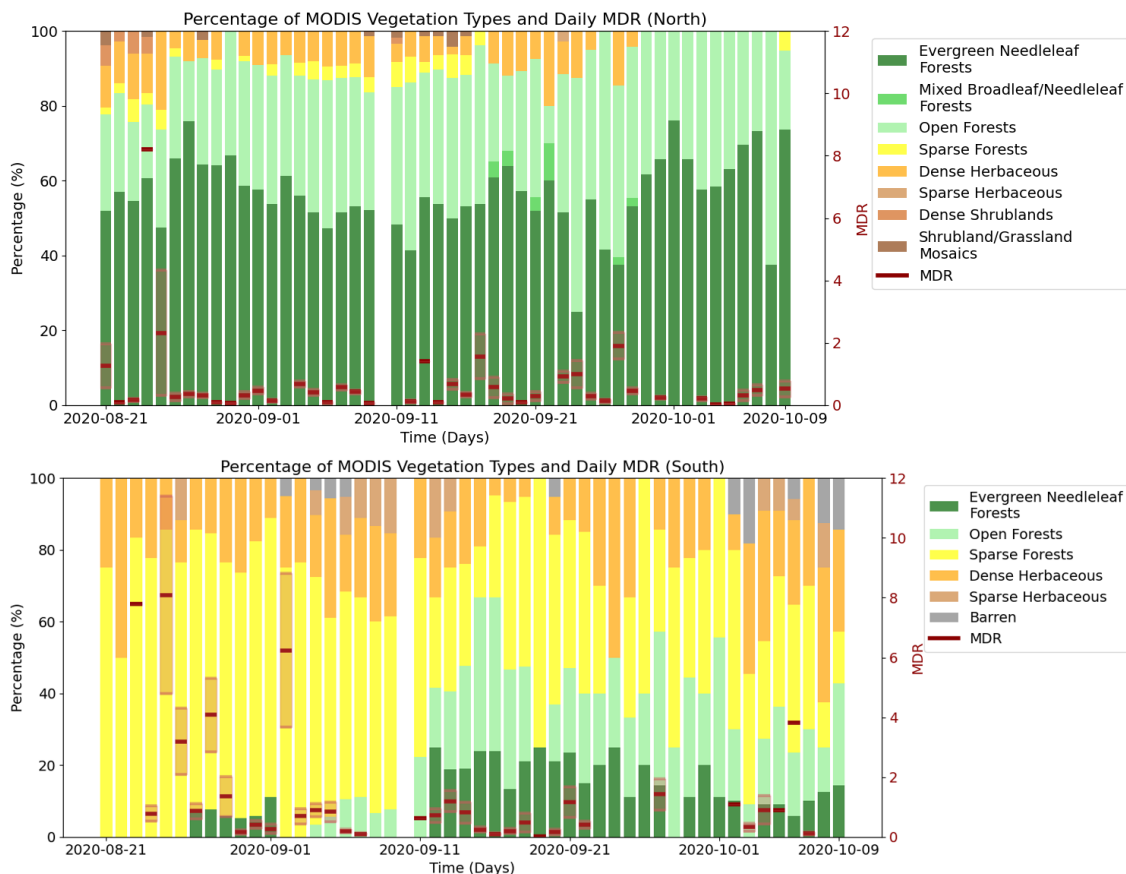


Figure 3.11: The image illustrates the percentage distribution of various MODIS vegetation types alongside daily average MDR in the northern and southern regions. The stacked bar chart shows the percentage of each vegetation type represented by various colours. Overlaid on each distribution, the red horizontal bars represent the average MDR value for that day, measured on the right Y-axis. The shaded region indicates the standard deviation values of the estimated MDR showcasing uncertainty in the measurement.

4

Discussion and Outlook

The first part of this work included estimating Mole Density Ratio (MDR), a proxy for combustion efficiency, using TROPOMI retrievals of NO_2 and CO during two major wildfires that occurred in the state of California, USA in the year 2020. The wildfire spanned a duration of 50 days, and the average MDR values, calculated over approximately 10-day intervals, were used to analyse the changes in MDR over time. The variation in MDR was more noticeable in the southern region compared to the northern regions. The reasons for such a difference was attributed to the dynamic landscape and the spread of fire through several types of vegetation in the southern region as explained in section 3.3.

Subsequently, MDR was estimated using super-observations of TROPOMI retrievals of NO_2 and CO at different resolutions. These estimated MDR values were then compared to those derived from TROPOMI retrievals in the first part of the work. In the northern areas, the MDR across all resolutions ranged between 0 and 1, whereas in the southern areas, it varied between 0 and 3. While the temporal trend in the variation of MDR across different fire periods remained consistent across the various resolutions, when comparing MDR across different resolutions, it was noticeable that the values varied significantly, particularly in the southern region. The MDR values derived from super-observations often did not align closely with those estimated using TROPOMI resolution. Substantial differences in certain observations suggest a loss of detail in estimation of MDR when super-observations are employed. As discussed in chapter 1, the study conducted by [22] observed a decrease in the $\Delta\text{NO}_2/\Delta\text{CO}$ ratio as the number of pixels in the analysis increased. This decrease is attributed to the chemical removal of NO_2 . Although they did not use the super-observation approach, some of the observed discrepancies could be attributed to change in number of pixels. Additional factors may also contribute to these discrepancies. For instance, the plume height of certain fires may exceed 10 metres. Consequently, using 10-metre wind data in this study could introduce uncertainties into the calculation of NO_2 and CO enhancements and thus affect the determination of MDR.

This was followed by the study of the potential link between MDR and environmental indicators. No definite conclusion could be drawn regarding the the effect of SPEI and SM on MDR change. While variations in drought conditions (indicated by SPEI values) and soil moisture values were observed across different fire periods and across both northern and southern regions, these variations did not correspond to changes in MDR (see Figure 3.7 and Figure 3.8). This suggests that several other factors influence MDR during wildfires, and the relationship between these environmental indicators and MDR requires further investigation to be clearly understood. For instance, vegetation with higher soil moisture content could result in a lower MDR compared to vegetation with lower soil moisture content.

Additionally, this study included analysing change in MDR in relation to change in vegetation type using GFED land use classification. This was repeated with the MODIS land use classification which is available at a much higher spatial resolution with a more extensive classification of vegetation types compared to the GFED. While the GFED data did not reveal any significant relationship between MDR and changes in vegetation in the northern region, MODIS data offered more detailed information regarding the correlation between MDR and vegetation types. In the southern region, the MDR values exhibited significant variation, which could clearly be correlated to changes in vegetation types. Higher MDR values were observed during periods with a higher percentage of less dense (grassland type of

vegetation) while periods with higher percentage of dense vegetation (forest type of vegetation) tend to have lower MDR values. This confirmed past studies which show that vegetation dominated by grassland is linked to flaming type of combustion and high MDR, while those dominated by forests are linked to smouldering type of combustion and low MDR. However, it remains challenging to definitively conclude whether the observed variations in MDR are primarily due to differences in the way of burning (flaming versus smouldering) or are instead due to changes in fuel type (variations in vegetation).

Finally, daily average MDR was utilised instead of the 10-day average to understand whether fluctuations in daily MDR could reflect changes in vegetation based on MODIS land use. It concluded that change in vegetation type is also reflected in daily variations in MDR to a certain extent. However, it is important to consider that factors other than vegetation, such as variation in winds, topography and the short lifetime of NO_2 could also contribute to daily variations in MDR. Furthermore, such an investigation is subject to sufficient data availability for reasonably accurate estimation of MDR.

While the current study demonstrated a loss of information on MDR when super-observations are employed and identified no correlation between MDR and SPEI or SM, the following potential research directions are proposed:

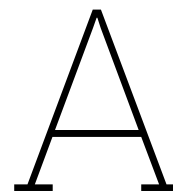
- Further investigation could involve producing super-observations in a different way. Instead of computing MDR using super-observations of NO_2 and CO, it could be worthwhile to create super-observations of MDR. However, the weights assigned to NO_2 and CO are potentially different due to variations in their pixel sizes, which could introduce complexity to this approach.
- The plume height of the fires could be estimated. As these plume heights typically exceed 10 metres, instead of using 10-metre wind data as used in this study, 100-metre wind data could be used to calculate the enhancements of NO_2 and CO, thereby reducing the uncertainty in MDR.
- The interplay between soil moisture variations and land cover types may also affect MDR. For instance, vegetation with higher soil moisture content could result in a lower MDR compared to dry vegetation. By integrating soil moisture variations with land cover classifications, the analysis can potentially improve the understanding of wildfire behaviour and its contribution to NO_2 and CO emissions.
- As discussed in section 3.1, several enhancements of NO_2 and CO in the southern region were zero. The current study samples the background at a distance of 30 km upwind from the fire in the southern region. Increasing this distance could help avoid sampling from the same grid cell. It would be valuable to conduct a study on the effects of altering this distance on combustion efficiency.
- While sampling background values of NO_2 and CO, wind directions may vary when the sampling distance is large. For instance, in the northern region, the background sampling locations, situated 90 km upwind, is likely to exhibit different wind directions compared to the wind over the fires, potentially resulting in uncertain background values. To further investigate this source of uncertainty, wind rose diagrams at the locations where background values are sampled could be created and compared with the wind rose diagrams at fire locations (see Figure A.3).
- Since different types of vegetation respond differently to droughts (see subsection 3.2.1), it is recommended that the Standardised Precipitation-Evapotranspiration Index (SPEI) aggregated over a 9-month period (SPEI-9) or a 12-month period (SPEI-12) be used for regions dominated by forest-type vegetation. Conversely, for areas primarily covered by grasslands, it is advisable to use SPEI aggregated over a shorter duration, such as a 1-month period (SPEI-1) or a 3-month period (SPEI-3). This approach will more accurately reflect the differing sensitivities of these vegetation types to drought conditions and its influence on combustion efficiency. Additionally, a higher spatial resolution dataset of SPEI and SM could perhaps shed more light and provide a more detailed analysis on their relationship with combustion efficiency.

References

- [1] Copernicus. *2023: A year of intense global wildfire activity*. Dec. 2023.
- [2] The Visual and Data Journalism Team. *California and Oregon 2020 wildfires in maps, graphics and images*. Sept. 2020.
- [3] UNEP. *Spreading like Wildfire: The Rising Threat of Extraordinary Landscape Fires*. Tech. rep. Geneva: United Nations Environment Programme, 2022, pp. 10–11. URL: https://wedocs.unep.org/bitstream/handle/20.500.11822/38372/wildfire_RRA.pdf.
- [4] Julien Ruffault et al. “Increased likelihood of heat-induced large wildfires in the Mediterranean Basin”. In: *Scientific Reports* 10.1 (2020). ISSN: 20452322. DOI: 10.1038/s41598-020-70069-z.
- [5] Alfonso Senatore et al. “Evaluating the uncertainty of climate model structure and bias correction on the hydrological impact of projected climate change in a Mediterranean catchment”. In: *Journal of Hydrology: Regional Studies* 42 (2022). ISSN: 22145818. DOI: 10.1016/j.ejrh.2022.101120.
- [6] John T. Abatzoglou and A. Park Williams. “Impact of anthropogenic climate change on wildfire across western US forests”. In: *Proceedings of the National Academy of Sciences of the United States of America* 113.42 (2016). ISSN: 10916490. DOI: 10.1073/pnas.1607171113.
- [7] U. Shankar et al. “Projecting wildfire emissions over the south-eastern United States to mid-century”. In: *International Journal of Wildland Fire* 27.5 (2018). ISSN: 10498001. DOI: 10.1071/WF17116.
- [8] M. O. Andreae and P. Merlet. “Emission of trace gases and aerosols from biomass burning”. In: *Global Biogeochemical Cycles* 15.4 (2001). ISSN: 08866236. DOI: 10.1029/2000GB001382.
- [9] R. L. Langenfelds et al. “Interannual growth rate variations of atmospheric CO₂ and its $\delta^{13}\text{C}$, H₂, CH₄, and CO between 1992 and 1999 linked to biomass burning”. In: *Global Biogeochemical Cycles* 16.3 (2002). ISSN: 08866236. DOI: 10.1029/2001gb001466.
- [10] Adam B. Smith and Richard W. Katz. “US billion-dollar weather and climate disasters: Data sources, trends, accuracy and biases”. In: *Natural Hazards* 67.2 (2013). ISSN: 0921030X. DOI: 10.1007/s11069-013-0566-5.
- [11] Neal Fann et al. “The health impacts and economic value of wildland fire episodes in the U.S.: 2008–2012”. In: *Science of the Total Environment* 610-611 (2018). ISSN: 18791026. DOI: 10.1016/j.scitotenv.2017.08.024.
- [12] Christina N. Vasilakopoulou et al. “Rapid transformation of wildfire emissions to harmful background aerosol”. In: *npj Climate and Atmospheric Science* 6.1 (2023). ISSN: 23973722. DOI: 10.1038/s41612-023-00544-7.
- [13] S. K. Akagi et al. “Emission factors for open and domestic biomass burning for use in atmospheric models”. In: *Atmospheric Chemistry and Physics* 11.9 (2011). ISSN: 16807324. DOI: 10.5194/acp-11-4039-2011.
- [14] Shawn Urbanski. “Wildland fire emissions, carbon, and climate: Emission factors”. In: *Forest Ecology and Management* 317 (Apr. 2014), pp. 51–60. ISSN: 03781127. DOI: 10.1016/j.foreco.2013.05.045.
- [15] Ivar R. Van Der Velde et al. “Biomass burning combustion efficiency observed from space using measurements of CO and NO₂ by the TROPOspheric Monitoring Instrument (TROPOMI)”. In: *Atmospheric Chemistry and Physics* 21.2 (Jan. 2021), pp. 597–616. ISSN: 16807324. DOI: 10.5194/acp-21-597-2021.
- [16] Kunpeng Yi and Yulong Bao. “Estimates of wildfire emissions in boreal forests of China”. In: *Forests* 7.8 (2016). ISSN: 19994907. DOI: 10.3390/f7080158.

- [17] Guido R. Van Der Werf et al. *Global fire emissions estimates during 1997-2016*. Sept. 2017. DOI: 10.5194/essd-9-697-2017.
- [18] J. P. Veefkind et al. "TROPOMI on the ESA Sentinel-5 Precursor: A GMES mission for global observations of the atmospheric composition for climate, air quality and ozone layer applications". In: *Remote Sensing of Environment* 120 (May 2012), pp. 70–83. ISSN: 00344257. DOI: 10.1016/j.rse.2011.09.027.
- [19] Muhammad A. Santoso et al. *Review of the Transition From Smouldering to Flaming Combustion in Wildfires*. 2019. DOI: 10.3389/fmech.2019.00049.
- [20] G Rein. "Smoldering combustion," in *SFPE Handbook of Fire Protection Engineering*. Ed. by D Gottuk et al. New York: NY: Springer New York, 2016, pp. 581–603.
- [21] Helene E Peiro, Alaina Kurt, and Sean Crowell. "Combustion efficiency observed with CO and NO₂ TROPOMI data: a first counties scale study during the 2020 fires of California Combustion efficiency observed with CO and NO₂ Héi ene Peiro". In: (2022). DOI: 10.1002/essoar.10511087.1. URL: <https://doi.org/10.1002/essoar.10511087.1>.
- [22] Lindsey D. Anderson et al. "Analyzing the Impact of Evolving Combustion Conditions on the Composition of Wildfire Emissions Using Satellite Data". In: *Geophysical Research Letters* 50.23 (Dec. 2023). ISSN: 19448007. DOI: 10.1029/2023GL105811.
- [23] ETF89. *Comoe Savannah fire*. Sept. 2015.
- [24] Violetta Ryabko. *The Russian wildfires in pictures*. Aug. 2019.
- [25] K. Miyazaki, H. J. Eskes, and K. Sudo. "Global NO_x emission estimates derived from an assimilation of OMI tropospheric NO₂ columns". In: *Atmospheric Chemistry and Physics* 12.5 (2012), pp. 2263–2288. ISSN: 16807316. DOI: 10.5194/acp-12-2263-2012.
- [26] T. Vincenty. "Direct and inverse solutions of geodesics on the ellipsoid with application of nested equations". In: *Survey Review* 23.176 (1975). ISSN: 17522706. DOI: 10.1179/sre.1975.23.176.88.
- [27] C. M. Thomas and W. E. Featherstone. "Validation of Vincenty's Formulas for the Geodesic Using a New Fourth-Order Extension of Kivioja's Formula". In: *Journal of Surveying Engineering* 131.1 (2005). ISSN: 0733-9453. DOI: 10.1061/(asce)0733-9453(2005)131:1(20).
- [28] Suvojit Sarkar and Debabrata Mondal. "Spatiotemporal changes in tropospheric nitrogen dioxide hotspot due to emission switch-off condition in the view of lockdown emergency in India". In: *Air Quality, Atmosphere and Health* 15.12 (Dec. 2022), pp. 2123–2135. ISSN: 18739326. DOI: 10.1007/s11869-022-01240-w.
- [29] Jos Van Geffen et al. "S5P TROPOMI NO₂ slant column retrieval: Method, stability, uncertainties and comparisons with OMI". In: *Atmospheric Measurement Techniques* 13.3 (2020). ISSN: 18678548. DOI: 10.5194/amt-13-1315-2020.
- [30] K. F. Boersma et al. "An improved tropospheric NO₂ column retrieval algorithm for the Ozone Monitoring Instrument". In: *Atmospheric Measurement Techniques* 4.9 (2011). ISSN: 18671381. DOI: 10.5194/amt-4-1905-2011.
- [31] Copernicus Atmospheric Mission Performance Cluster Service. *Copernicus Atmospheric Mission Performance Cluster Service Quarterly Validation Report of the Copernicus Sentinel-5 Precursor Operational Data Products #21: April 2018-November 2023*. Tech. rep. 2023, pp. 7–9. URL: <https://mpc-vdaf.tropomi.eu/ProjectDir/reports//pdf/S5P-MPC-IASB-ROCVR-21.01.00.pdf>.
- [32] Tobias Borsdorff et al. "Monitoring CO emissions of the metropolis Mexico City using TROPOMI CO observations". In: *Atmospheric Chemistry and Physics* 20.24 (2020). ISSN: 16807324. DOI: 10.5194/acp-20-15761-2020.
- [33] Jochen Landgraf et al. "Carbon monoxide total column retrievals from TROPOMI shortwave infrared measurements". In: *Atmospheric Measurement Techniques* 9.10 (Oct. 2016), pp. 4955–4975. ISSN: 18678548. DOI: 10.5194/amt-9-4955-2016.
- [34] Sergio M. Vicente-Serrano, Santiago Beguería, and Juan I. López-Moreno. "A multiscalar drought index sensitive to global warming: The standardized precipitation evapotranspiration index". In: *Journal of Climate* 23.7 (Apr. 2010), pp. 1696–1718. ISSN: 08948755. DOI: 10.1175/2009JCLI2909.1.

- [35] Santiago Beguería et al. "Standardized precipitation evapotranspiration index (SPEI) revisited: Parameter fitting, evapotranspiration models, tools, datasets and drought monitoring". In: *International Journal of Climatology* 34.10 (2014). ISSN: 10970088. DOI: 10.1002/joc.3887.
- [36] CT Agnew. "Using the SPI to identify drought". In: *Drought Networks News* 12.1 (2000).
- [37] Climate Data Store Copernicus Climate Change Service. *Soil moisture gridded data from 1978 to present*. 2018. DOI: 10.24381/cds.d7782f18. URL: <https://cds.climate.copernicus.eu/cdsapp#!/dataset/10.24381/cds.d7782f18?tab=overview>.
- [38] Alexander Gruber et al. "Triple Collocation-Based Merging of Satellite Soil Moisture Retrievals". In: *IEEE Transactions on Geoscience and Remote Sensing* 55.12 (2017). ISSN: 01962892. DOI: 10.1109/TGRS.2017.2734070.
- [39] G. R. Van Der Werf et al. "Global fire emissions and the contribution of deforestation, savanna, forest, agricultural, and peat fires (1997-2009)". In: *Atmospheric Chemistry and Physics* 10.23 (2010), pp. 11707–11735. ISSN: 16807324. DOI: 10.5194/acp-10-11707-2010.
- [40] M. Friedl and D Sulla-Menashe. "MODIS/Terra+Aqua Land Cover Type Yearly L3 Global 500m SIN Grid V061 [Data set]." In: *NASA EOSDIS Land Processes Distributed Active Archive Center* (2022).
- [41] L Giglio. "MOD14A1 MODIS/Terra thermal anomalies/fire daily L3 global 1 km SIN grid V006". In: *NASA EOSDIS Land Processes DAAC, doi 10* (2015).
- [42] Jeff Dozier. "A method for satellite identification of surface temperature fields of subpixel resolution". In: *Remote Sensing of Environment* 11.C (1981). ISSN: 00344257. DOI: 10.1016/0034-4257(81)90021-3.
- [43] M. Matson and J. Dozier. "Identification of subresolution high temperature sources using a thermal IR sensor." In: *Photogrammetric Engineering and Remote Sensing* 47.9 (1981). ISSN: 00991112.
- [44] H. Hersbach et al. "ERA5 hourly data on single levels from 1940 to present. Copernicus Climate Change Service (C3S) Climate Data Store (CDS), DOI: 10.24381/cds.adbb2d47 (Accessed on 06-Sep-2023)". In: *Ecmwf* 147 (2023). ISSN: 14783576.
- [45] Anzhou Zhao et al. "Responses of vegetation productivity to multi-scale drought in Loess Plateau, China". In: *Catena* 163 (2018). ISSN: 03418162. DOI: 10.1016/j.catena.2017.12.016.



Appendix

A.1. Data Summary

An investigation on the dataset was conducted to attain a more detailed understanding of the results (see Figure A.1 and Figure A.2).

Reasons for Masked Values: Low-quality pixels, such as those affected by clouds, shadows, or other forms of invalid data, are excluded from analysis to ensure the accuracy and reliability of the results. For instance, TROPOMI employs quality assurance values for pollutants like nitrogen dioxide (NO₂) and carbon monoxide (CO). If the data falls below the established quality assurance thresholds, it is systematically excluded from the analysis. This practice is crucial in remote sensing and atmospheric studies to avoid inaccuracies that could arise from poor-quality measurements.

Reasons for Negative Values: Orography may significantly influence the observed data, particularly in regions with varied terrain, such as the south. In such areas, fire can spread across different elevations, leading to complex interactions between the terrain and pollutant dispersion. In certain cases, the background concentration of pollutants might be sampled from valleys, where pollutant accumulation can be higher compared to areas directly affected by the fire. Consequently, this can result in negative enhancement values, where the measured pollutant concentration in the fire-affected area is lower than the background levels. Understanding these topographical influences is essential for accurately interpreting pollutant data in heterogeneous landscapes. Furthermore, negative NO₂ enhancements were more frequent than those of negative CO enhancements. Nearby urban/industrial areas could possibly have higher levels of NO₂ compared to the fires, especially during the end of the fires leading to more number of negative values of NO₂ enhancements compared to CO enhancements.

Reasons for Zero Values: Frequent zero values in the southern region indicate that the distance of 30 km used for sampling background values of NO₂ and CO could mean sampling data from the same grid cell as the fire. This results in a significant proportion of NO₂ and CO enhancement concentrations being zero. This is especially true for higher resolutions evident by the increase in the number of zero data points as super-observation resolution increases from 0.3°×0.3° to 0.5°×0.5°. While in the northern region the distance used for sampling is 90 km which ensures that sampling is not done from the same grid cell as the fire.

Since NaN, negative and zero values are excluded from the MDR calculations, the counts of unique positive and positive data points represent the available data for these calculations.

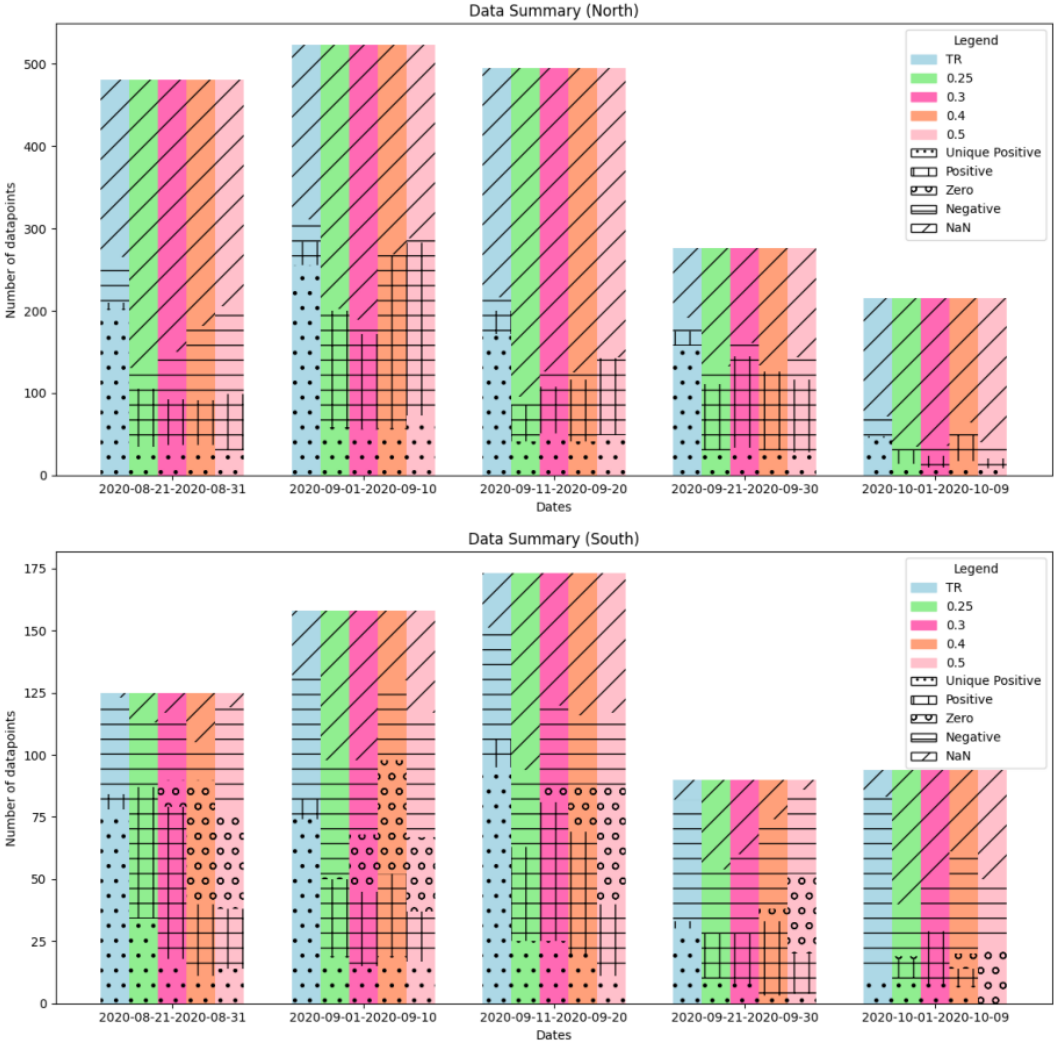


Figure A.1: Data Summary : The figure presents a comparative summary of data points for the northern (top) and southern (bottom) regions. Each bar represents the number of data points within specific date ranges, subdivided by resolutions and categories of data type, indicated in the legend. The shading and patterning within the bars distinguish these categories: Nan, negative, zero, positive and unique positive values. Different colours represent different resolutions, providing a visual representation of the distribution and variability of data across the defined periods for both regions.

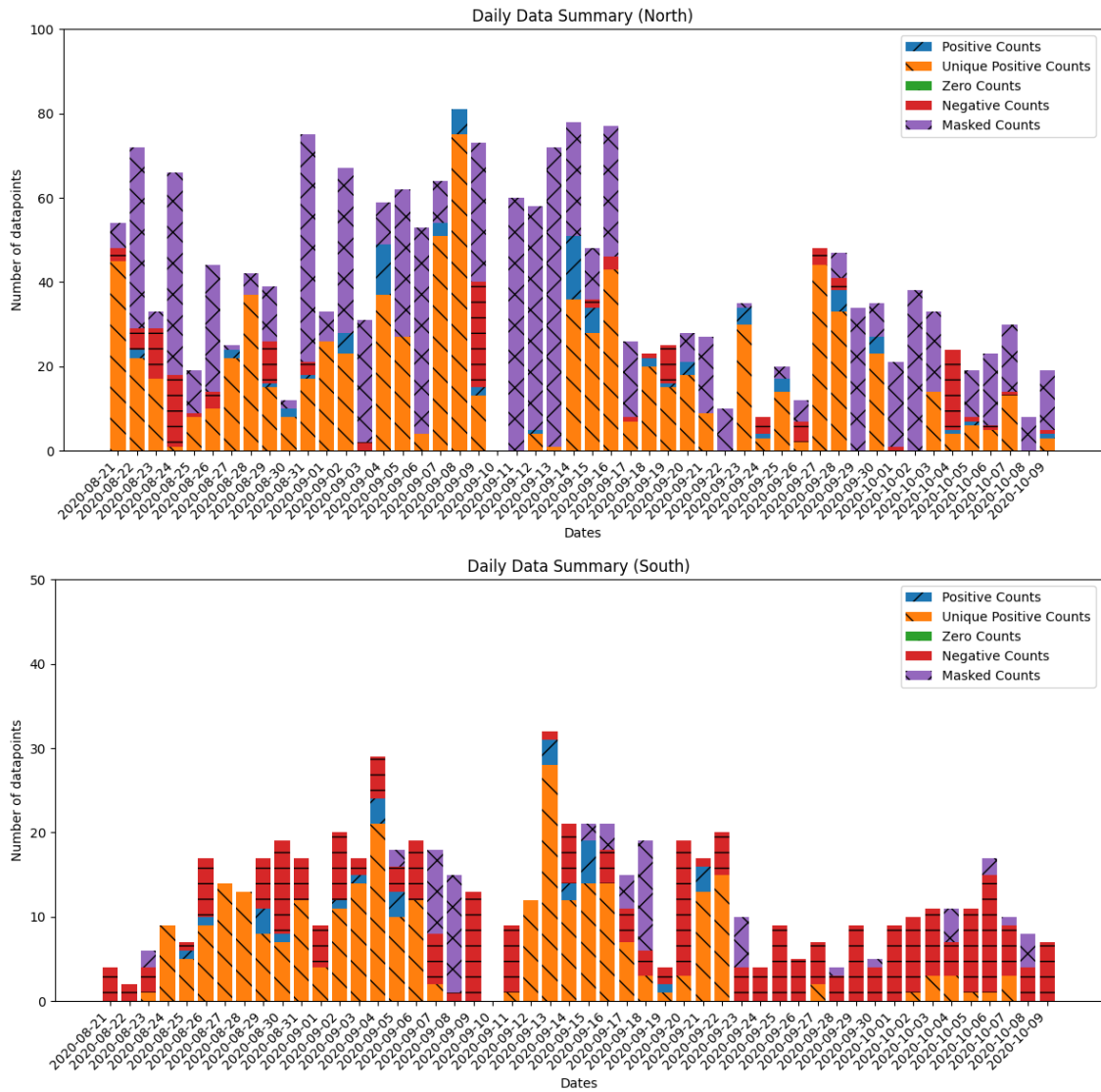


Figure A.2: Daily Data Summary for TROPOMI resolution : The figure presents a summary of data points for the northern (top) and southern (bottom) regions. Each bar represents the count of different data types recorded on each day. This summary aids in understanding the data availability and quality for each day, highlighting days with insufficient data for an unreliable MDR estimation.

A.2. Monte Carlo Simulation

Monte Carlo simulations uses random sampling to compute results. In the context of this study, such random sampling helps in understanding the day to day variability of NO₂ and CO. By executing several iterations, a more accurate estimate of the expected value and variability of the MDR can be achieved. Each iteration involves sampling a subset of NO₂ and CO enhancements. Following sampling, the means of these subsets are computed, and their ratio is taken to determine the MDR. This process is repeated 10,000 times, resulting in 10,000 MDR values. Subsequently, a simple arithmetic mean and standard deviation of these MDR values are calculated.

A.3. Wind Rose Diagrams

A wind rose is a graphical tool used to visualise how wind speed and direction are distributed at a particular location over a specified time period. These wind rose diagrams are circular with the directions (N, NE, E, SE, S, SW, W, NW) marked around the circumference. The variations in wind directions between the two regions is also noticeable. The subplots on the left, corresponding to the northern region and depicted in blue, illustrate a higher variation in wind direction compared to the southern region subplots on the right, shown in red (see Figure A.3).

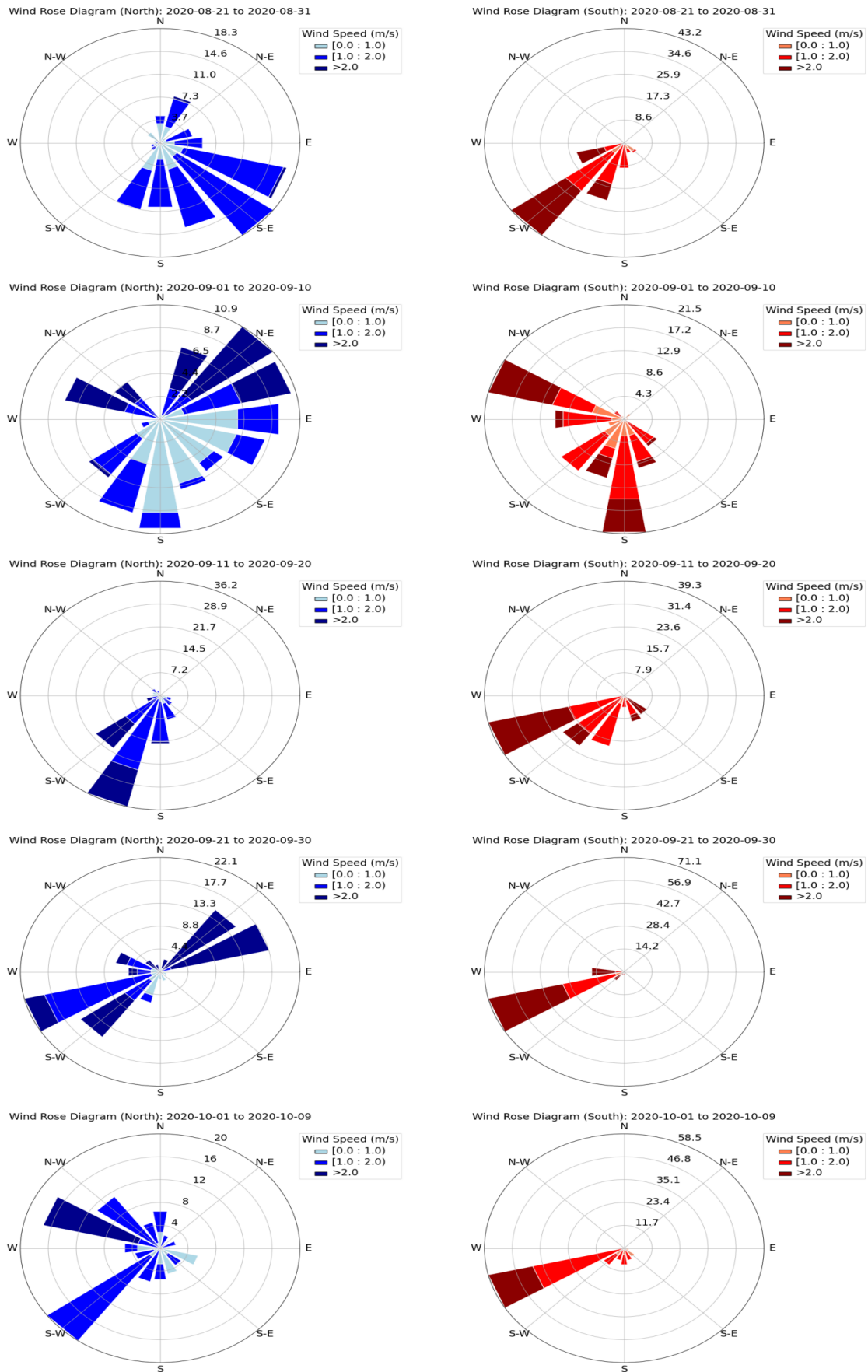


Figure A.3: Period wise Wind Rose Diagrams for the northern and the southern regions. The concentric circles provide a scale for frequency, marked at various intervals while the wind speeds are colour coded with blue for winds in the northern region and red for winds in the southern region with darker shades representing higher wind speeds. For example, the top most wind rose diagram on the right for the southern region (2020-08-21 to 2020-08-31) has the longest bar reaching the 43.2 mark suggests that winds from the SW direction were the most frequent, with speeds mostly above 2.0 m/s.